



Calhoun: The NPS Institutional Archive DSpace Repository

Theses and Dissertations

1. Thesis and Dissertation Collection, all items

1992-12

Very low frequency signals and whistler-mode amplification in the magnetosphere and limit-cycle behavior in the CEBAF infrared free electron laser

Caudle, Daryl L.

Monterey, California. Naval Postgraduate School

<http://hdl.handle.net/10945/24103>

This publication is a work of the U.S. Government as defined in Title 17, United States Code, Section 101. Copyright protection is not available for this work in the United States.

Downloaded from NPS Archive: Calhoun



<http://www.nps.edu/library>

Calhoun is the Naval Postgraduate School's public access digital repository for research materials and institutional publications created by the NPS community. Calhoun is named for Professor of Mathematics Guy K. Calhoun, NPS's first appointed -- and published -- scholarly author.

Dudley Knox Library / Naval Postgraduate School
411 Dyer Road / 1 University Circle
Monterey, California USA 93943



D. KNOX LIBRARY
NEW POSTGRADUATE SCHOOL
MONTEREY CA 93943-5101

REPORT DOCUMENTATION PAGE

1a. REPORT SECURITY CLASSIFICATION UNCLASSIFIED		1b. RESTRICTIVE MARKINGS	
2a. SECURITY CLASSIFICATION AUTHORITY		3. DISTRIBUTION/AVAILABILITY OF REPORT Approved for public release; distribution is unlimited.	
2b. DECLASSIFICATION/DOWNGRADING SCHEDULE			
4. PERFORMING ORGANIZATION REPORT NUMBER(S)		5. MONITORING ORGANIZATION REPORT NUMBER(S)	
6a. NAME OF PERFORMING ORGANIZATION Naval Postgraduate School		6b. OFFICE SYMBOL (if applicable) 33	7a. NAME OF MONITORING ORGANIZATION Naval Postgraduate School
6c. ADDRESS (City, State, and ZIP Code) Monterey, CA 93943-5000		7b. ADDRESS (City, State, and ZIP Code) Monterey, CA 93943-5000	
8a. NAME OF FUNDING/SPONSORING ORGANIZATION		8b. OFFICE SYMBOL (if applicable)	9. PROCUREMENT INSTRUMENT IDENTIFICATION NUMBER
8c. ADDRESS (City, State, and ZIP Code)		10. SOURCE OF FUNDING NUMBERS	
		Program Element No.	Project No.
		Task No.	Work Unit Accession Number
11. TITLE (Include Security Classification) VERY LOW FREQUENCY SIGNALS AND WHISTLER-MODE AMPLIFICATION IN THE MAGNETOSPHERE AND LIMIT-CYCLE BEHAVIOR IN THE CEBAF INFRARED FREE ELECTRON LASER			
12. PERSONAL AUTHOR(S) Daryl L. Caudle			
13a. TYPE OF REPORT Master's Thesis	13b. TIME COVERED From	14. DATE OF REPORT (year, month, day) December 1992	15. PAGE COUNT 114
16. SUPPLEMENTARY NOTATION The views expressed in this thesis are those of the author and do not reflect the official policy or position of the Department of Defense or the U.S. Government.			
17. COSATI CODES		18. SUBJECT TERMS (continue on reverse if necessary and identify by block number) whistler-mode amplification, Siple Station VLF Signals, saturation, exponential growth, synchrotron oscillation, triggered emission, resonance, taper, limit-cycle behavior, wave-particle interaction, slippage distance, desynchronization, FEL	
19. ABSTRACT (continue on reverse if necessary and identify by block number) Very low frequency (VLF) electromagnetic wave injection experiments were conducted on 23-24 January 1988 from a 42-km horizontal dipole antenna located at Siple Station, Antarctica. The experiment consisted of a diagnostic format transmitted from one minute every five minutes for a 10 hour period between 1700 UT and 0300 UT. These signals were received and recorded at the conjugate magnetic field point location at Lake Mistissini, Canada. A detailed analysis of this data clearly demonstrates hot plasma effects such as saturated power levels, exponential growth rates, sideband formation and triggered emissions due to wave-particle interactions. These hot plasma effects remain constant over a time scale of 30 seconds but show large variations over a time scale of 5 minutes. These VLF signals were used to simulate "whistler waves" which occur naturally and are amplified by energetic electrons spiraling around magnetic field lines near the geomagnetic equator. Navy VLF communications are strongly affected by the presence of whistler waves. The electron and whistler wave interaction can be described by a theoretical model which is very similar to that used for free electron lasers (FEL). Using computer simulation, most of the hot plasma effects seen in the Siple Station data can be modeled and compared to FEL characteristics such as saturation, electron trapping, tapering, and sensitivity to energy distributions. Two dimensional computer simulations in coordinates z and t have predicted that the CEBAF Infrared (IR) FEL can observe limit-cycle behavior when operating within its design parameters. The IR FEL is driven by a high quality electron beam with a micropulse length comparable to the slippage distance. At moderate values of the desynchronization, the optical power will oscillate periodically over several hundred passes through the resonator. The limit-cycle power oscillations are caused by "marching subpulses" that grow at the trailing edge of the optical pulse through a super-radiant process and pass through the main optical envelope.			
20. DISTRIBUTION/AVAILABILITY OF ABSTRACT <input checked="" type="checkbox"/> UNCLASSIFIED/UNLIMITED <input type="checkbox"/> SAME AS REPORT <input type="checkbox"/> DTIC USERS		21. ABSTRACT SECURITY CLASSIFICATION UNCLASSIFIED	
22a. NAME OF RESPONSIBLE INDIVIDUAL W. B. Colson		22b. TELEPHONE (Include Area code) 408-656-2765	22c. OFFICE SYMBOL PH/Cw

**VERY LOW FREQUENCY SIGNALS AND WHISTLER-MODE
AMPLIFICATION IN THE MAGNETOSPHERE AND LIMIT-CYCLE
BEHAVIOR IN THE CEBAF INFRARED FREE ELECTRON LASER**

by

Daryl L. Caudle

Lieutenant, United States Navy
B.S., North Carolina State University, 1985

Submitted in partial fulfillment of the
requirements for the degree of

MASTER OF SCIENCE IN PHYSICS

from the

NAVAL POSTGRADUATE SCHOOL

December, 1992

ABSTRACT

Very low frequency (VLF) electromagnetic wave injection experiments were conducted on 23-24 January 1988 from a 42-km horizontal dipole antenna located at Siple Station, Antarctica. The experiment consisted of a diagnostic format transmitted for one minute every five minutes for a 10 hour period between 1700 UT and 0300 UT. These signals were received and recorded at the conjugate magnetic field point location at Lake Mistissini, Canada. A detailed analysis of this data clearly demonstrates hot plasma effects such as saturated power levels, exponential growth rates, sideband formation and triggered emissions due to wave-particle interactions. These hot plasma effects remain constant over a time scale of 30 seconds but show large variations over a time scale of 5 minutes. These VLF signals were used to simulate "whistler waves" which occur naturally and are amplified by energetic electrons spiraling around magnetic field lines near the geomagnetic equator. Navy VLF communications are strongly affected by the presence of whistler waves.

The electron and whistler wave interaction can be described by a theoretical model which is very similar to that used for free electron lasers (FEL). Using computer simulation most of the hot plasma effects seen in the Siple Station data can be modeled and compared to free electron laser characteristics such as saturation, electron trapping, tapering, and sensitivity to energy distributions.

Two dimensional computer simulations in coordinates z and t have predicted that the CEBAF Infrared (IR) FEL can observe limit-cycle behavior when operating within its design parameters. The IR FEL is driven by a high quality electron beam with a micropulse length comparable to the slippage distance. At moderate values of the desynchronization, the optical power will oscillate periodically over several hundred passes through the resonator. The limit-cycle power oscillations are caused by "marching subpulses" that grow at the trailing edge of the optical pulse through a super-radiant process, and pass through the main optical envelope.

TABLE OF CONTENTS

I.	INTRODUCTION	1
II.	MOTIVATION FOR THE STUDY OF WHISTLERS AND FREE ELECTRON LASERS	4
	A. NAVY VLF COMMUNICATION AND NAVIGATION SYSTEMS	4
	B. EFFECTS OF WHISTLERS ON VLF SIGNALS	6
	C. SHIPBOARD USE OF THE FREE ELECTRON LASER	8
III.	VLF WAVE-INJECTION EXPERIMENTS FROM SIPLE STATION, ANTARCTICA	11
	A. THE MAGNETOSPHERE	11
	B. SIPLE STATION EQUIPMENT AND ANTENNA DESCRIPTION	15
	C. DUCTED VLF WAVE PROPAGATION THEORY	18
	D. SIPLE STATION TRANSMITTED FREQUENCY FORMAT	20
IV.	ANALYSIS OF SIPLE STATION DATA FROM 23-24 JANUARY 1988	22
	A. WHY WAS THIS DATA SET CHOSEN?	22
	B. RECEIVED FREQUENCY AND AMPLITUDE INFORMATION	26
	1. Exponential Growth	28
	2. Saturated Power Level	29
	3. Sidebands	32
	4. Triggered Emissions	33
	5. Magnetospheric Events	35
	C. THE THRESHOLD POWER CONCEPT	37
	1. Background	37
	2. Determining the Threshold Power	40
	3. Temporal and Spatial Wave Growth	43
	4. A Sample Calculation	43

V. WHISTLER AND VLF WAVE-PARTICLE INTERACTION THEORY	46
A. THE COLD BACKGROUND PLASMA.....	46
B. THE WAVE EQUATION	50
C. THE HOT ELECTRON EQUATIONS OF MOTION	52
D. TAPER AND THE PENDULUM EQUATION.....	57
1. Taper	57
2. The Pendulum Equation	57
VI. SIMULATIONS AND DISCUSSION	59
A. SOLVING THE HOMOGENEOUS EQUATIONS OF MOTION.....	59
1. Weak VLF Fields and Low Gain.....	60
2. Weak VLF Fields and High Gain	61
3. Strong VLF Fields and High Gain.....	62
B. SOLVING THE INHOMOGENEOUS EQUATIONS OF MOTION	66
1. Mono-Energetic Electron Beam in a Tapered Magnetic Field	66
2. Gaussian Distributed Electron Beam in a Tapered Magnetic Field.....	69
VII. LIMIT-CYCLE BEHAVIOR IN THE CEBAF INFRARED FREE ELECTRON LASER (FEL).....	71
A. FEL DESIGN AND OPERATION	71
B. DESCRIPTION OF THE CEBAF IR FACILITY	72
C. THE CEBAF IR FEL DESIGN	73
D. LIMIT-CYCLE BEHAVIOR	75
E. SIMILARITIES BETWEEN FELS AND WHISTLER-MODE AMPLIFICATION (WMA).....	84
VIII. SUGGESTIONS FOR FUTURE WORK	86
A. FURTHER ANALYSIS OF SIPLE STATION DATA	86
B. IMPROVEMENTS TO THE SIMULATION	86

C. MORE ON LIMIT-CYCLE BEHAVIOR.....	87
IX. CONCLUSIONS.....	89
APPENDIX A. ATLAS OF WHISTLER AND TRIGGERED EMISSION TYPES [REF. 2].....	92
APPENDIX B. SAMPLE CALCULATION OF EXPERIMENTAL PARAMETERS IN THE INTERACTION REGION USING MATHCAD 3.1®	94
APPENDIX C. PERFORMANCE CALCULATION OF THE SIPLE STATION HORIZONTAL DIPOLE ANTENNA USING MATHCAD 3.1®.....	99
LIST OF REFERENCES.....	102
INITIAL DISTRIBUTION LIST	105

ACKNOWLEDGMENT

The author gratefully acknowledges the guidance and support of Dr. W. B. Colson. The author also wishes to thank V. S. Sonwalkar, D. L. Carpenter, and R. A. Helliwell of Stanford University, for the all of their instruction and motivation. Finally, the author would like to thank his loving wife, Mona, and daughter, Gillian, for their patience, support, and assistance while writing this thesis.

I. INTRODUCTION

The study of "whistlers" began with the earliest days of radio communication. Whistlers are tones that sweep over many frequencies within the audio range and sound like whistles or musical type signals. At the time, prior to World War I, whistlers were heard, but their origin was not known. Then in 1919, Barkhausen officially published the first account of whistlers while studying the currents in the earth's ionosphere. Between 1930 and 1935, Barkhausen and Eckersley wrote a paper describing the theory of whistling atmospherics in great detail [Ref. 1]. They said, "Whistlers originate from impulsive atmospherics, or lightning, and travel through the outer ionosphere, following the lines of force of the earth's magnetic field and crossing over the equator at great heights." [Ref. 1] Even then, they knew that the dispersion measurements of whistlers yielded information about the density of electrons in the ionosphere.

These originally published experimental observations lacked supporting theoretical computations, until L. R. O. Storey published his work on whistlers in 1952. Storey performed a systematic study of whistlers over many years before making conclusions about the variations of whistler properties. Then, he formulated and published the first theoretical work on the dispersion relationship, group velocity, and time-delays due to field-aligned ducted propagation of a whistler. Finally, in 1965, R. A. Helliwell published the first comprehensive book on whistlers that incorporated both experimental observations and theoretical explanations for most ionospheric phenomena [Ref. 2].

The study of whistlers has long been a topic of concern for the military. Some of the first reports of whistlers came from Germans attempting to listen to Allied telephone conversations during World War I [Ref. 2]. Since then, whistlers have been a problem to communication lines and navigation systems as described in Chapter II.

In order to better understand whistlers, Siple Station was built in Antarctica in 1972. This station was used to transmit very low frequency (VLF) signals along field-aligned

magnetospheric ducts which were received at Lake Missiniti, Canada. These VLF signals were used to simulate the properties of whistlers and their propagation paths in a controlled fashion. Chapter III describes the experiment and equipment used at Siple Station. Also included in Chapter III is a brief description of the magnetosphere and the Van Allen Belt electron properties.

Chapter IV begins with a detailed study of frequency and amplitude information received from Siple Station on 23-24 January 1988. Examples of single and multi-path propagation are shown, and the theory behind ducted propagation is presented. Examples of triggered emissions from the transmitted signals are shown and defined. Characteristic properties of the wave-particle interaction between the VLF wave and the hot plasma electrons are presented. These include exponential growth of the VLF signals, saturation of the VLF signals, sideband formation after saturation, and triggered emissions at signal termination. The concept of threshold power and the use of Siple Station signals as a hot plasma diagnostic tool are presented.

In Chapter V, a theory is developed to explain the amplification of the VLF signals in the inhomogeneous magnetosphere. The whistler mode dispersion relationship is derived from Maxwell's equations and the cold electron current. Then the VLF wave equation is developed by including the hot electron current in Maxwell's equations. Finally, the self-consistent motion of each hot electron is described by solving the Lorentz force equation driven by the VLF wave and the earth's inhomogeneous magnetic field. Amplification of the VLF signal occurs because of a gyro-resonant condition between the wave and counter-streaming hot electrons with energies of ≈ 1 keV. This interaction occurs in a hypothetical region at the geomagnetic equator along the field line of interest in the magnetosphere. The interaction region is ≈ 1000 km long and a few degrees of latitude wide. Chapter V concludes with a parallel made between whistler amplification and the free electron laser (FEL). This discussion includes the idea of a "tapered" interaction and the electron pendulum equation that results from a homogeneous geomagnetic field.

In Chapter VI, the equations of motion for each hot electron are solved simultaneously with the VLF wave equation using computer simulations. These equations are numerically integrated given an appropriate set of initial conditions. Chapter VI includes simulations for a variety of initial conditions illustrating the effects of gain, saturation, the trapped-particle instability and the inhomogeneous magnetic field. The simulations are able to produce most of the effects seen in the actual experimental data with the exception of triggered emissions. Equations that have traditionally been used to predict and distinguish the regions of high and low gain, and strong and weak fields for FELs are tested on the VLF wave simulations. Finally, the effects of an initial electron energy spread are shown for tapered and non-tapered scenarios.

Chapter VII deviates from the world of geophysics and enters the world of free electron lasers. In this chapter, a short pulse effect, known as limit-cycle behavior, is predicted to occur in the Continuous Electron Beam Acceleration Facility (CEBAF) infrared (IR) FEL. Limit-cycle behavior is the result of a super-radiant process that occurs when the electron pulse length is comparable to the slippage distance. This process causes the optical power to oscillate even though all operational parameters are held constant. This chapter concludes with a comparison between whistler interactions and free electron lasers.

In Chapter VIII, suggestions for improving the VLF wave simulations are made. The major area of improvement includes the incorporation of more realistic distributions describing the hot electron's energy and pitch angle.

II. MOTIVATION FOR THE STUDY OF WHISTLERS AND FREE ELECTRON LASERS

A. NAVY VLF COMMUNICATION AND NAVIGATION SYSTEMS

"Whistlers" are very low frequency (VLF) radio signals in the audio-frequency range that resemble a "whistle" [Ref. 2]. Whistlers are characterized by their large sweep in frequency over a short time period. A typical whistler can sweep 500 Hz in one second. Whistlers can be heard over most audio frequency radio equipment and even long runs of telephone line. They are typically initiated by strokes of lightning and propagate in both the earth's ionosphere and magnetosphere. The density of whistler signals is dependent on the time of day, the earth's magnetic activity, location on earth and the weather. Whistlers are more common at mid-latitudes and because of poor propagation conditions are not observed at the equator nor the poles. The waveform of a whistler is sketched in Figure 2-1a. Also shown in Figure 2.1b, is a simple sketch of the usual way whistlers are displayed with frequency along the vertical axis and time along the horizontal axis. A complete description of all known whistler types is found in Appendix A. [Ref. 2]

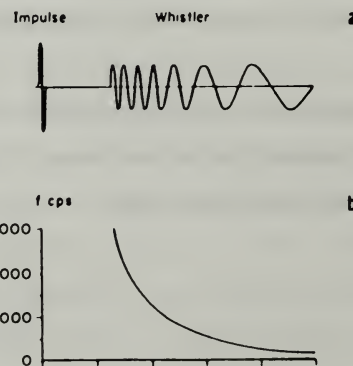


Figure 2-1. Idealized waveform (a) and spectrum of a whistler (b). [Ref. 2]

Because the Navy depends heavily on VLF signals, the study of whistlers is warranted. The Navy uses VLF radio signals as its primary means for long range communication with submarines. Because of the long wavelengths involved, VLF signals can travel large distances with low attenuation in the earth-ionospheric waveguide and can penetrate sea water to a depth of 10 to 30 feet. Therefore, VLF is used extensively as the primarily means of transmitting everything from the news to nuclear release orders to submarines. There are many VLF transmitting stations in the United States. They are listed in Table 1-1. [Ref. 3]

TABLE 1-1. VLF TRANSMITTERS.

Call Sign	Transmitter	Frequency	Latitude	Longitude
NSS	USN Maryland	21.4 kHz	39° N	76° W
NPM	USN Hawaii	23.4 kHz	21° N	158° W
NAU	USN Puerto Rico	28.5 kHz	18° N	67° W
NAA	USN Maine	24.0 kHz	45° N	67° W
NLK	USN Washington	24.8 kHz	48° N	122° W

Not only are VLF signals used for communications, they are also used extensively for long range navigation systems. Both Loran and Omega are navigation systems that operate in the VLF, medium frequency (MF), and low frequency (LF) bands. Loran-A, originally devised during World War II, operates at 1850-1950 kHz with a range of approximately 450 to 800 nautical miles (nm) by day and up to 1400 nm at night [Ref. 4]. Loran-C operates at 90 to 110 kHz so that both ground wave and sky wave modes are possible [Ref. 5]. The ground wave mode has a range of approximately 1200 nm and the sky wave mode with two reflections can be received up to 4000 nm.

Omega operates at 10 to 14 kHz. Since this system operates at very low frequencies, it has an effective range of 5000 to 6000 nm and can penetrate sea water so that

submarines can use it at periscope depth. Atomic clocks are required to synchronize the transmitted and received signals. Only eight stations are necessary to cover the entire globe, with three stations being accessible at any location. [Ref. 4]

B. EFFECTS OF WHISTLERS ON VLF SIGNALS

As stated earlier whistlers are initiated by lightning discharges known as "spherics" which are impulsive in nature. Spherics themselves constitute a major impediment to VLF navigation and communication system as a source of intensive static or noise. Suppose that a transmitter is sending out a VLF signal with constant amplitude, and a receiver, some distance away, is receiving the signal. Typically, the wave energy will propagate in the earth-ionosphere waveguide, interacting with the two boundaries in a manner that is dependent on the electrical properties of the two boundaries. This is illustrated in Figure 2-2 [Ref. 6]. Because the electrical properties, such as the conductivity and the relative permittivity remain essentially constant over many seconds or minutes, the signal strength remains essentially constant and may be synchronized and received.

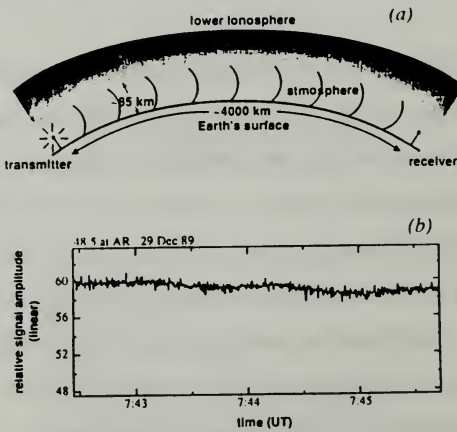


Figure 2-2. Schematic representation of a VLF signal (top) propagating under ambient conditions with the relative signal strength shown (bottom) [Ref. 6].

When sudden (< 1s) or impulsive changes in one or the other waveguide boundaries occur, the amplitude and the phase of the signal beyond the disturbance also suddenly changes. This can be a significant problem when binary data is being transmitted. A sudden change in the lower boundary (i.e. the ground or water) is not as likely, and will not be considered here. A sudden change in the upper boundary occurs frequently, and is caused by solar flares or by energetic electrons being dislodged from the radiation belts. When a whistler or a manmade VLF signal is launched, it can enter the magnetosphere via a ducted mode discussed in Chapter III and interact with gyro-resonant electrons. During this interaction, the electrons give up energy to the VLF wave and amplify it. If sufficient energy is transferred, the electron cannot sustain its original orbit, and is precipitated out of the magnetosphere into the ionosphere. Figure 2-3 (top) schematically illustrates this type of disturbance. The disturbance grows in size as the precipitated electrons cause secondary ionizations where they slow down. Figure 2-3 (bottom) shows a typical VLF signature disturbed by a lightning-induced ionospheric disturbance.

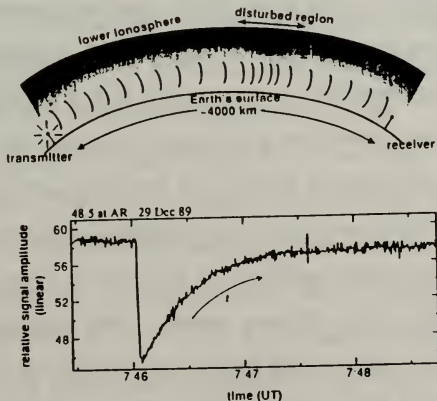


Figure 2-3. Schematic diagram of a perturbed ionosphere (top) and a typical VLF signature after a lightning-induced disturbance (bottom) [Ref. 6].

The disturbed region recovers back to its ambient state after approximately 100 s. This characteristic signature is commonly referred to as a "Trimpie event", consisting of a quick (<1 s) perturbation followed by a relatively slow (\approx 100 s) recovery.

Therefore, whistlers can affect Naval VLF signals directly and indirectly. Directly, they can initiate and sweep over transmitted frequencies resulting in low signal-to-noise ratios at the receiving station. Since they are VLF also, they can travel large distances and cause communication problems over a large area. Indirectly, whistlers can enter the magnetosphere where they can interact with electrons in the Van Allen Belt causing them to precipitate. This precipitation can cause Trimpie events which form "pimples" on the upper ionosphere waveguide boundary that can disrupt communications for many seconds. This thesis concentrates on the magnetospheric interaction between electrons and manmade VLF signals, which are used to simulate whistlers.

C. SHIPBOARD USE OF THE FREE ELECTRON LASER

With the current threat of third world arms proliferation and the uncertainty surrounding the breakup of the Soviet Union, many new countries are achieving the capability of launching cruise and ballistic missiles capable of reaching the United States and its allies. Sophisticated point defense systems such as the Patriot missile (ground-based) or the Phalanx Close-In Weapon System (ship based) are not good enough to defend against new and improved tactical cruise missiles that are capable of 10 g terminal jinking maneuvers. These new missiles could be defended against with a defensive missile of roughly 3 times the maneuverability or 30 g's; however, this same technology would eventually be applied to the offensive weapon. The escalating "see-saw" between offensive and defensive kinetic energy missiles is not practical nor achievable. Therefore, the need for a speed of light weapon is obvious. The question becomes, "What type of speed of light weapon is best suited to fit the needs of the Navy?"

The answer is, of course, a laser. After, the Strategic Defense Initiative (SDI) started in the early 1980's, both neutral and charged particle beams were proven to be inefficient methods of transporting energy through the atmosphere. This left the laser as the only viable option. Currently, two types of laser systems are under development that are capable of generating the necessary power for defensive purposes. They are the mid-infrared advanced chemical laser (MIRACL) and the free electron laser (FEL). High energy lasers (> 1 MW) can effectively counter high speed and quick reaction targets. A missile traveling Mach 2 at a range of 5 km would only close 5.7 mm during the time it takes the light to reach it. Typical dwell times required to destroy an incoming missile are on the order of 2 seconds. This has obvious advantages over the tracking and homing limitations of conventional counter-defense missiles.

The Mid-Infrared Advanced Chemical Laser (MIRACL) at White Sands Missile Range is a deuterium fluoride (DF) chemical reaction laser. The laser output, at $3.8\text{ }\mu\text{m}$, is rated for powers greater than 1 MW. The laser burns NF_2 and D_2 to produce excited DF*. The reaction takes place in a resonant optical cavity that couples the coherent radiation as the DF* de-excites. The DF gases are exhausted from the cavity using steam ejectors. This by-product gas is acidic and highly toxic. Successive testing of the MIRACL system has been conducted against supersonic drones.

On the other hand, the FEL is another high power laser design with many advantages over the chemical laser. The FEL uses a relativistic beam of high energy electrons as the lasing source [Ref. 7]. Unlike conventional lasers or chemical lasers, a FEL is not a device based on atomic transitions. The electrons radiate as they "wiggle" through a periodic magnetic field. Therefore, there is no limit to the magazine depth since the supply of electrons is endless. It will be shown in Chapter VII, that the wavelength of a FEL is proportional to the squared inverse of the electron beam energy. Therefore, the FEL's output is tunable over many wavelengths just by adjusting the electron beam energy. FELs have demonstrated output wavelengths from the infrared (IR) to the ultraviolet

(UV). The advantages of having a tunable laser are numerous. The optimal wavelength can be selected so that atmospheric degradation is minimized, and missile skin damage is maximized. Finally, compared to a chemical laser, the FEL is a clean weapon. Electrons are much more manageable than a hot, acidic DF gas. Therefore, shipboard personnel are at less risk while the FEL is operating.

There are, however, some problems that the FEL must overcome before it could be placed onboard a ship. Even though FELs have high peak powers (GW) [Ref. 8], none have demonstrated the high average power required for a ship-based weapon. Second, the FEL and support equipment require a large amount of space. Therefore, it would be impossible to place the system on an existing surface combatant. Finally, to operate a FEL with an output of 2 MW and a wallplug efficiency of 20%, the system would require 10 MW of electrical power. This load would be too large for the onboard turbine generators. Therefore, new electrical distribution equipment would have to be designed. However, all electrical-drive ship designs, recently being considered, could easily transfer electrical propulsion power over to the FEL. Even with these drawbacks, the FEL is a young and promising technology that deserves the Navy's attention.

III. VLF WAVE-INJECTION EXPERIMENTS FROM SIPLE STATION, ANTARCTICA

A. THE MAGNETOSPHERE

In order to understand how radio waves and whistlers are amplified, it is imperative to accurately describe the environment in which they propagate. The terms and illustrations developed in this chapter are important in order to understand the experimental and theoretical concepts developed later. Throughout this thesis, the earth's geomagnetic field is assumed to equal the field produced by a perfect dipole magnet. This of course is not exactly true because of the solar wind. The magnetosphere is broken into two regions separated by a boundary known as the magnetopause. The geomagnetic field lines all close inside the magnetopause. This boundary separates the region where the earth's magnetic field is closely approximated by a dipole from the region where the action of the solar wind strongly distorts the earth's field. The region outside the magnetopause is known as the magnetosheath. A bow shock wave forms on the sun side of the earth as the solar wind causes the magnetosphere to be compressed. As the solar wind passes over and around the magnetosphere, a "tail" is formed which has been observed to stretch out over hundreds of earth radii. Figure 3-1 illustrates the magnetosphere components and how the solar wind distorts the shape. [Ref. 9]

By concentrating on regions inside the magnetosphere, the dipole magnetic field approximation is applicable and accurate. This region changes size depending on the time of day, time of year, solar activity, and particle injection events. This region includes the plasmasphere which is made up of a "cold" background plasma that determines the bulk properties of the media and a "hot" plasma which makes up the earth's Van Allen radiation belts. The cold background plasma consists of electrons and protons ranging in energy from approximately 0.1 to 1 eV. Their concentration can be described by diffusive

equilibrium models with densities ranging from about 10,000 particles/cm³ at ionosphere heights (\approx 1000 km) to about 200-400 particles/cm³ at the plasmasphere boundary. The plasmasphere boundary, called the plasmapause, was discovered by using naturally occurring whistler waves and is characterized by a significant decrease in cold plasma density [Ref. 10].

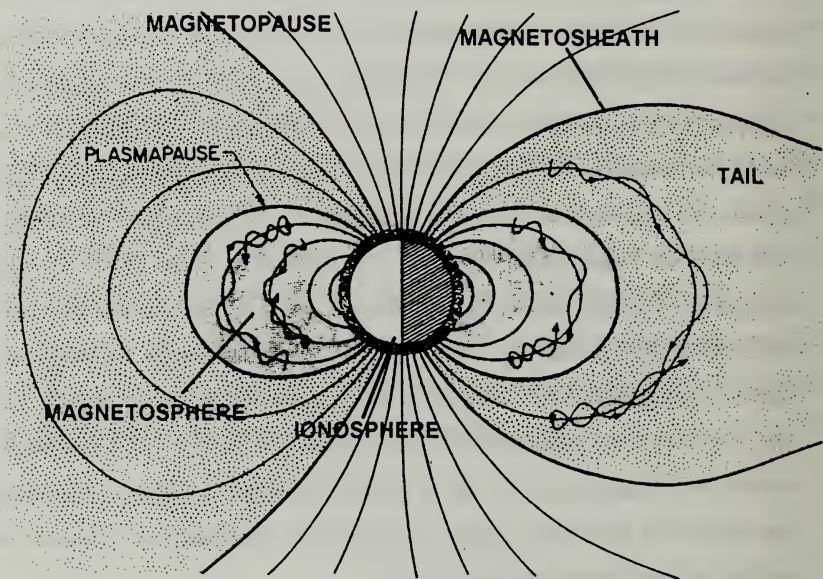


Figure 3-1. A schematic diagram of the earth's magnetic field demonstrating the components of the magnetosphere.

The hot plasma includes electrons and protons having energies ranging from about 1 keV to 100 MeV which are trapped in helically precessed orbits illustrated in Figure 3-2. These energetic particles follow the magnetic field lines and bounce between magnetic conjugate points. As the particles move away from the equator their kinetic energy is

transferred from parallel velocity components to perpendicular velocity components. A convenient parameter to monitor during a particle's trajectory is its pitch angle,

$$\alpha = \tan^{-1} \left(\frac{V_{\perp}}{V_{\parallel}} \right) \quad (3.1)$$

where α is the angle between the particle's perpendicular velocity, V_{\perp} , and its parallel velocity, V_{\parallel} [Ref. 11]. Therefore, the particle's pitch angle increases as it moves away from the equator until it equals 90° , and then bounces and heads the other way. The "bounce latitude" for a particular particle is determined by knowing its pitch angle at any particular latitude on its path. The particles also precess around the earth because the magnetic field is non-uniform, since it gets stronger closer to the earth. Therefore, the particles spiral in non-symmetric helical paths that "walk" or "drift" around the earth.

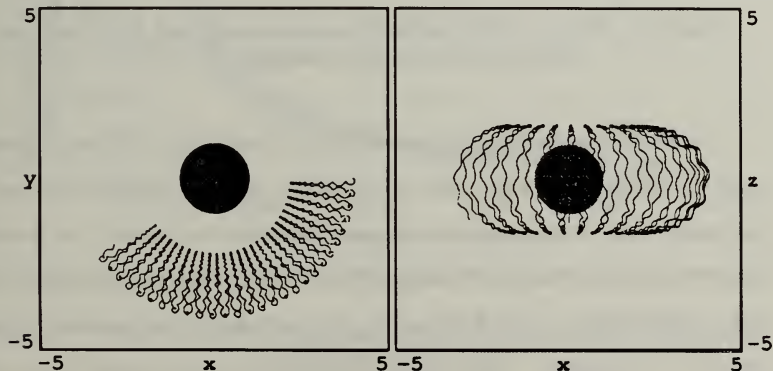


Figure 3-2. Example of one electron's bounce (right) and drift motion (left) in a dipole field where distances are in earth radii.

A detailed example demonstrating the formulation of these dynamics can be found in Appendix B. Typical bounce periods for 1.5 keV electrons range from 4 to 7 seconds and

typical drift periods range from 40 to 60 hours. Figure 3-3 plots the bounce period and the drift period for a 1.5 keV electron versus its equatorial pitch angle.

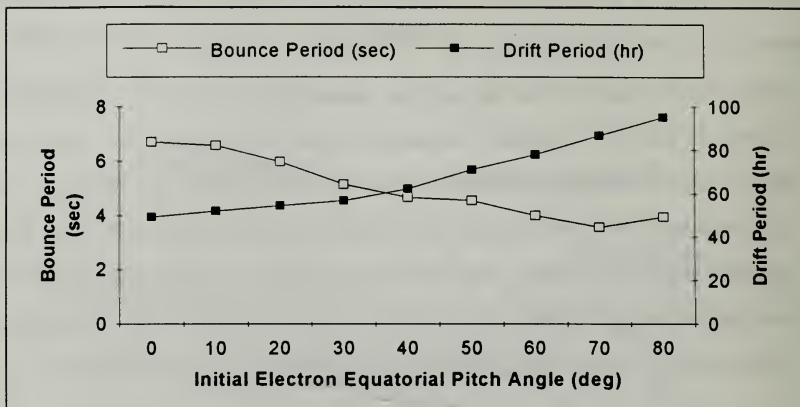


Figure 3-3. Plot of a 1.5 keV electron's bounce period and drift period versus the electron's initial equatorial pitch angle at $L = 5.1$.

If an electron has a sufficiently low pitch angle at the equator, it will travel far enough down its respective field line to enter the ionosphere. Once the electron has entered the ionosphere, it can easily interact with many positively charged ions where it can chemically bond or lose enough energy from collisions that it will not bounce and return along a field line. These electrons are lost from the Van Allen belts due to this depletion mechanism known as "precipitation". This limiting equatorial pitch angle subtends a solid angle known as the "loss cone" within which there are no electrons. For a given equatorial pitch angle, an electron will travel a certain distance into the ionosphere. Figure 3-4 plots the equatorial pitch angle an electron must have for a given L -shell to reach an altitude of $h = 1000$ km. This "loss height" is somewhat arbitrary but agrees with experimental observation [Ref. 11]. The equatorial loss cone pitch angle is insensitive to changes in h .

as Figure 3-4 also illustrates. The L -shell, or the McIlwain L -parameter, is a convenient way to describe a given magnetic field line in terms of the radial distance at which the field line crosses the geomagnetic equator,

$$L = \frac{R_{eq}}{R_o} \quad (3.2)$$

where R_{eq} is the radial distance to the geomagnetic equator and R_o is the mean radius of the earth (6370 km). [Ref. 11] The details of Figure 3-4 formulation are also presented in Appendix B.

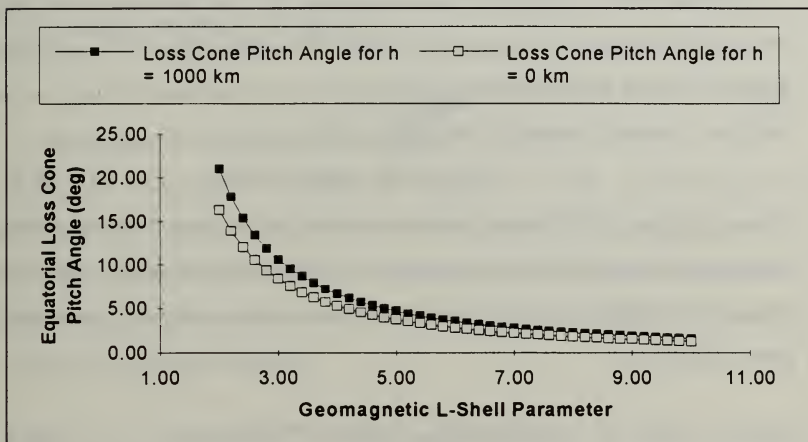


Figure 3-4. Plot of the electron equatorial loss cone pitch angle versus L -shell where h is the ionospheric loss height.

B. SIPLE STATION EQUIPMENT AND ANTENNA DESCRIPTION

Very-low-frequency (VLF) transmissions began in Antarctica in 1965 with a 33.6-kilometer (km) dipole laid on the ice at Byrd Station (68.2° S, $L=7.25$). This facility was used jointly by Stanford University and the University of Washington [Ref. 12]. However, the geomagnetic latitude of Byrd Station was too high for receiving ducted transmissions

in the conjugate hemisphere [Ref. 13]. Accordingly, a lower latitude site (60.8°S , $L=4.2$) was selected where a 21-km horizontal dipole antenna and a VLF transmitter were placed in operation in 1972 at Siple Station. The receiving and recording station was located at Lake Missiniti, Canada. This antenna, with a resonant frequency of 5.1 kHz, was used to diagnose the magnetosphere for eleven years. In 1983, a new 42-km horizontal dipole antenna with a one-half resonant frequency of 2.49 kHz was put into operation. This longer, lower wavelength antenna had its resonant frequency in the center of the 1-4 kHz band that had been found to be ideal for wave injection experiments [Ref. 14].

In January 1983, current and voltage measurements for the 42-km antenna were made for the second resonance frequency of 7.75 kHz. The current distribution throughout the antenna allows the ideal transmitted power to be computed assuming the earth is a lossy flat plane. The vector potential for the horizontal dipole antenna is computed using,

$$\bar{A} = \bar{A}_x (e^{ikh \cos(\theta)} + R_h(\theta) e^{-ikh \cos(\theta)}) \quad (3.3)$$

where \bar{A}_x is the complex vector potential amplitude in the x-direction, k is the wave number, h is the antenna height above ground, R_h is the reflection coefficient, and θ is the polar angle in spherical coordinates [Ref. 15]. The complex vector potential amplitude is given by [Ref. 15]

$$\bar{A}_x = \hat{x} \frac{\mu e^{-ikr}}{4\pi r} \int_{-L/2}^{L/2} I(x) e^{ikx \sin(\theta) \cos(\theta)} dx \quad (3.4)$$

where \hat{x} is a unit vector in the x-direction, μ is the permeability of the propagation medium, r is the far-field radial distance from the center of the antenna, and $I(x)$ is the current distribution along the antenna. Once the vector potential is calculated, the electric, \bar{E} , and magnetic, \bar{H} , fields are obtained and expressed in spherical coordinates as [Ref. 15]

$$\bar{E} = -i\omega (A_\theta \hat{\theta} + A_\phi \hat{\phi}) \quad (3.5)$$

and

$$\bar{H} = \frac{1}{\eta} \hat{r} \times \bar{E} \quad (3.6)$$

where ω is the wave frequency and η is the intrinsic impedance of the medium. The Poynting vector follows from the cross product of the real parts of the electric and magnetic fields. In this case, the magnitude of the time-averaged Poynting vector, $|\bar{S}|$, simplifies to

$$|\bar{S}| = \frac{1}{2\eta} \bar{E} \cdot \bar{E}^* \quad (3.7)$$

where the $*$ denotes the complex conjugate. The Poynting vector magnitude is integrated over the upper hemisphere of the antenna,

$$P = \iint_{\substack{\text{upper} \\ \text{hemisphere}}} |\bar{S}| dA \quad (3.8)$$

to yield the total power, P , emitted by the antenna. Table 3-1 below gives the characteristics of the Siple Station 42-km antenna. [Ref. 12] The radiated powers are calculated numerically using Table 3-1 and Equations (3.3) through (3.8) [Appendix C]. The radiated powers in Table 3-1 are consistent with the values reported by the STAR Laboratory at Stanford University.

TABLE 3-1. PROPERTIES OF THE 42-km ANTENNA AT SIPLE STATION, ANTARCTICA

Frequency (kHz)	Impedance (Ω)	Attenuation Constant (Np/m)	Phase Constant (rad/m)	Phase Velocity (m/s)	Radiated Power (kW)
2.49	75	1.4E-5	7.5E-4	2.09E8	≈ 1.7
7.75	415	1.8E-5	2.2E-4	2.17E8	≈ 0.31
13.40	770	4.5E-5	3.7E-4	2.20E8	≈ 0.17

C. DUCTED VLF WAVE PROPAGATION THEORY

In order for whistler waves or VLF signals to interact with counter-streaming electrons in the magnetosphere, they must follow the same magnetic field lines for an extended distance. Typically when a RF wave is launched, either naturally or manmade, some of the signal is trapped in the earth-ionosphere waveguide while the rest escapes into space depending on the local index of refraction, incidence angle and many other factors. However, measurements made at conjugate magnetic receiving stations, show that RF waves can travel along "ducts" which form around magnetospheric field lines [Ref. 2]. Duct propagation was primarily determined first by the delay time measurements made at the receiving station since the launch time was known.

Electromagnetic waves bend in response to changes in the index of refraction and the index of refraction changes as the local electron density fluctuates. Therefore, the anisotropy of the ionosphere and magnetosphere at very low frequencies can act to guide the path of propagation approximately in the direction of the static magnetic field. Evidence has shown that for non-ducted VLF signals, the wave-normal angle becomes too large and exceeds the critical angle for total internal reflection. In that case only a weak evanescent signal would be received on the ground. [Ref. 2]

To discuss the theory of VLF wave trapping, a ray tracing duct model is used. The duct is formed by enhancements in the index of refraction caused by the electron density profile. A useful parameter for studying ducting is the ratio of the whistler wave frequency to the electron gyro-frequency, $\Lambda = \omega / \Omega$. A special condition occurs when the wave frequency is one-half the electron gyro-frequency, $\Lambda = 0.5$. The phase and group velocities are equal and the entire character of propagation changes. Most whistler and triggered emission phenomena occur near this frequency for reasons not well understood. Figure 3-5 illustrates the ducting ray traces for "crest trapping" and "trough trapping." In

these two figures, $N(0)$ is the electron density on the axis of the irregularity and $N(P)$ is the electron density at the outermost excursion of the ray path from the axis. The local magnetic field direction is given by H_0 . [Ref. 2]

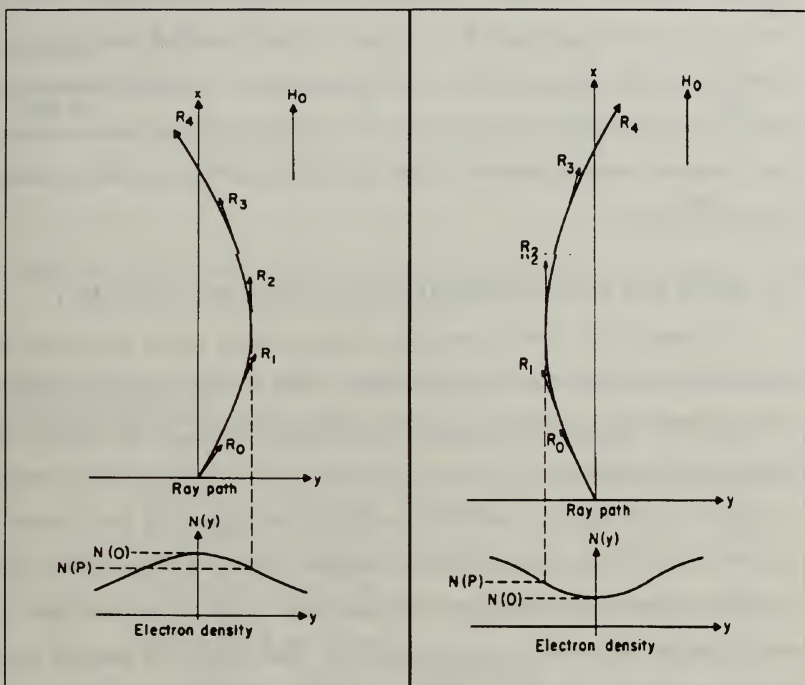


Figure 3-5. Ray trace in a field aligned irregularity. Crest trapping, $0 < \Lambda < 0.5$ (left) and trough trapping, $0.5 < \Lambda < 1.0$ (right).

The need for ducted propagation was based on three observations of ground-based whistlers. (1) A whistler which is excited by a lightning flash appears as a series of discrete frequencies with shapes that are independent of the location of the lightning source and location of the receiver. This result establishes that the paths of propagation

are fixed in the magnetosphere and ionosphere and are a characteristic of the medium only. (2) The second observation is closely related to the first and is based on whistler echoes. Frequently, a whistler is observed to echo and the separation time of the echoes for a given frequency is constant. This suggests that the signal follows the same path each time it traverses the magnetosphere. (3) Finally, if a fully developed, well-defined nose whistler is carefully analyzed, it fits, within experimental error, the theoretical predictions based on purely longitudinal propagation. This close agreement between the shape of each trace and the predictions of the purely longitudinal theory requires that the paths be field aligned. [Ref. 2]

D. SIPLE STATION TRANSMITTED FREQUENCY FORMAT

On January 23-24, 1988 a diagnostic frequency format lasting one minute was transmitted from Siple Station every five minutes. This format consisted of a series of fixed frequency pulses, frequency ramps, and parabolas between 1.9 kHz and 2.9 kHz. The format was centered at the resonance frequency of 2.45 kHz for the 42-km antenna. In addition to the frequency variations, transmitted power was either held constant or ramped with a constant slope for some of the signals. Finally, in all cases but two, the signals were right-hand circularly polarized and in those two special cases, one signal was left-handed and the other was linearly polarized. Each signal was designed with a particular experiment in mind in order to probe the different characteristics of the magnetosphere. In the next chapter, a detailed study of the macroscopic properties of each signal is presented. From this analysis, conclusions are drawn about the properties of the magnetospheric duct these signals propagated. Figure 3-6 illustrates the transmitted format with frequency (kHz) versus time (sec) during transmission and Table 3-2 gives the details about each signal.

HR241 SIPLE TRANSMITTER FORMAT

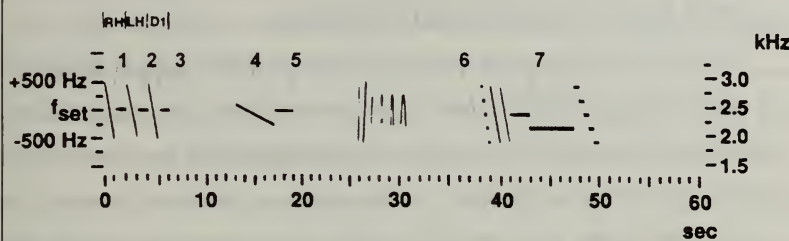


Figure 3-6. Example of the HR241 Siple Station diagnostic format. The center frequency is 2.45 kHz.

TABLE 3-2. HR241 SIPLE TRANSMITTER FORMAT AND SIGNAL CHARACTERISTICS.

Signal	Frequency (kHz)	Power Level	Polarization	Signal Length (sec)	Time Transmitted
1a	2.4 \pm .5 ramp	10 dB/sec for 1/2 sec	Right Hand	1	0:00
1b	2.4 constant			1	0:01
2a	2.4 \pm .5 ramp	10 dB/sec for 1/2 sec	Left Hand	1	0:02
2b	2.4 constant			1	0:03
3a	2.4 \pm .5 ramp	10 dB/sec for 1/2 sec	Linear	1	0:04
3b	2.4 constant			1	0:05
4	2.4 \pm .25 ramp	constant	Right Hand	4	0:13
5	2.4 constant	constant	Right Hand	2	0:17
6	2.4 constant	constant	Right Hand	200 msec	0:38.5
7	2.4 constant	10 dB/sec for 1 sec	Right Hand	2	0:41

IV. ANALYSIS OF SIPLE STATION DATA FROM 23-24 JANUARY 1988

A. WHY WAS THIS DATA SET CHOSEN?

Between 1700 UT (universal time) on 23 January to 0300 UT on 24 January 1988, the HR241 format described in Chapter III was transmitted from Siple Station, Antarctica. This data set was selected from thousands of hours of transmitted data because of many desirable characteristics. First of all, most signals that are transmitted from such a long non-directional antenna excite many ducts. This occurs because poor directivity allows many transmission angles to receive significant RF power. Also, the dispersive ionosphere can bend and scatter signals into many magnetospheric ducts. Therefore, the receiving Station receives signals that may have propagated through many ducts with different delay times. This is called "multipath" propagation as illustrated in Figure 4-1. In this figure, the top panel shows a whistler that propagated over three distinct paths with three distinct reception time delays. This is usually not desired because it is difficult to analyze what happen in just one duct. The bottom panel shows a pure, single-path whistler with its echo approximately one second later. This data set showed little multipath propagation over the ten hour period.

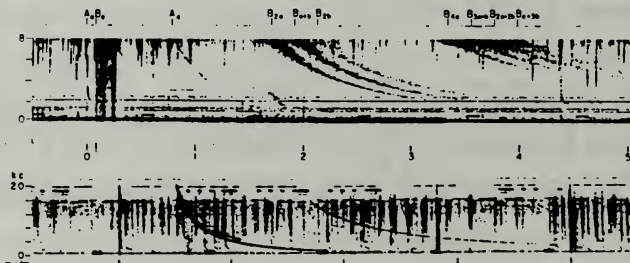


Figure 4-1. Example of a multipath whistler (top) versus a single-path whistler (bottom). Frequency is along the vertical axis and time is along the horizontal axis [Ref. 2].

To compare data that spans over a ten hour period, it is important that all signals traverse the same duct and stay in the same duct. This is determined by first observing single-path propagation and second, measuring the signal delay time. The signal delay time is the time difference between transmission and reception. Consistently throughout the ten hour period, the delay time of each signal was four seconds. This was true when different signals were compared to each other within the one minute transmission period and when the same signals were compared to each other after each five minute off period.

These data were also interesting because of some atypical time variations in the type and number of signals received. Moreover, there was an extremely low density of triggered emission activity observed during this ten hour period. It is important and helpful to graphically study a few examples: (1) There were times during a one minute transmission that only frequency ramped signals were received and a few cases when only constant frequency signals were received as illustrated in Figure 4-2 and 4-3.

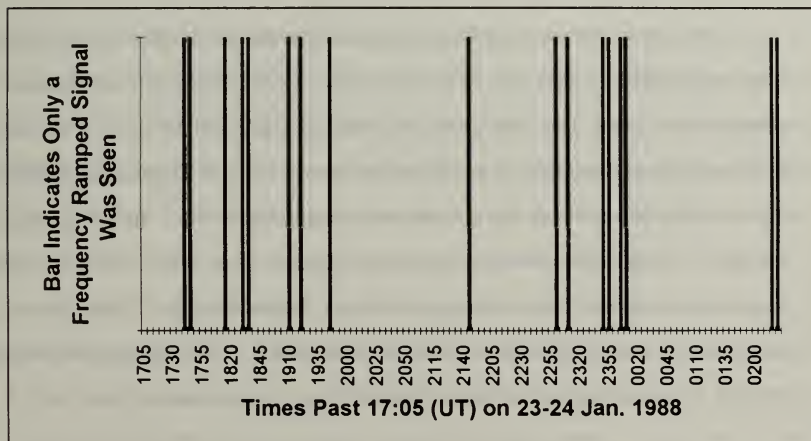


Figure 4-2. Times during the one minute transmission period when **only** ramped frequency signals were received.

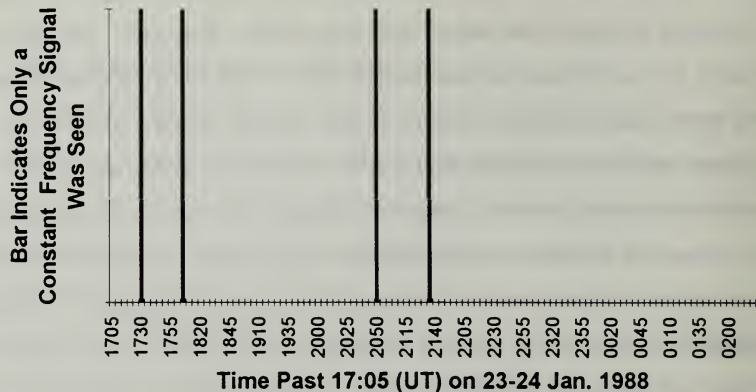


Figure 4-3. Times during the one minute transmission period when **only** constant frequency signals were received.

At the present, there is no theory or adequate explanation to describe why one type of frequency profile was preferentially amplified and received. When this rare behavior is observed, it is more likely that a frequency ramped signal will be seen. This occurs because the signal is sweeping over a large frequency band which increases the probability that the VLF wave will find a suitable resonance condition with the interacting hot electrons. (2) Within a one minute transmission period, there was a total of 13 signals transmitted. The total number of signals received at Lake Missiniti, Canada out of 13 transmitted varied significantly over the ten hour period. The percentage of signals received in a one minute period over the ten hour time scale is shown in Figure 4-4.

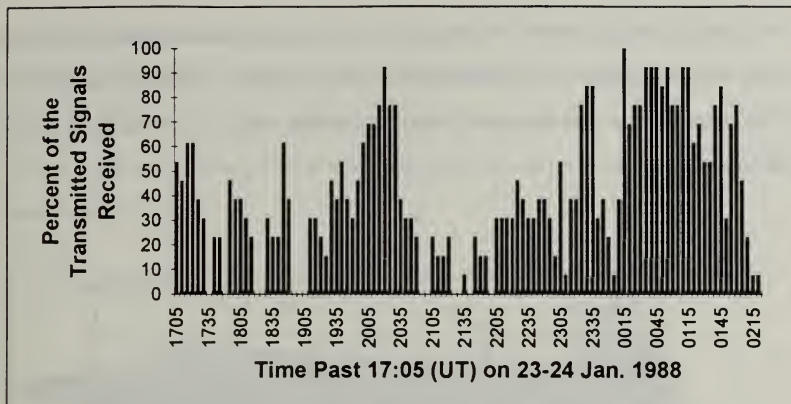


Figure 4-4. Percentage of the total signals received in a one minute transmission period.

Using Figure 4-4 as a guide, an hour and a half window starting at 00:15 (UT) was chosen to be studied in more detail because of the large percentage of transmitted signals received during this period. Even over a one minute time scale not all signals of the same type were received. Therefore, the mechanism for amplification can change abruptly during the one minute transmission period. However, Figures 4-2 and 4-3 depict that this was usually not the case. One has to factor in that these signals may or may not be at the same initial power (see Table 3-2) when analyzing Figure 4-4. (3) Finally, it is typical for Siple data to be plagued with many triggered emission signals sprouting off transmitted signals. "A triggered emission is any emission that appears to have been initiated, or triggered, by another event or interaction such as whistlers, discrete emissions, or signals from VLF transmitters [Appendix A]." Emissions can easily sweep fifty percent of their initiation frequency and usually arrive in multiple ducts. Figure 4-5 demonstrates a transmitted signal with rising and falling triggered emissions emanating from it. However, the data received during the discussed ten hour period had a very low density of triggered emissions and all but a very few cases the emissions were single-path. Again, this made

analyzing this data set easier. The triggered emissions usually occurred at the termination of the transmitted signal and demonstrated very pure frequency sweeps with no sidebands. These rare characteristics demanded a closer and in-depth study of the data set from 23-24 January, 1988.

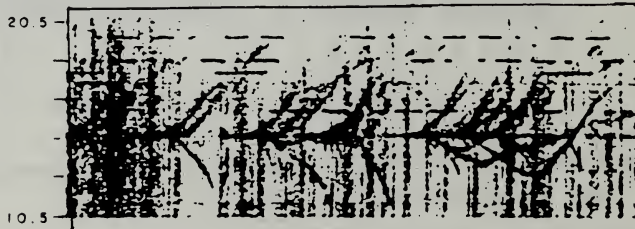


Figure 4-5. An example of rising and falling triggered emissions [Ref. 2].

B. RECEIVED FREQUENCY AND AMPLITUDE INFORMATION.

The receiving station recorded all of the data on magnetic analog tapes that are stored at Stanford University. This raw data was processed with a 100-Hz band pass filter around the center frequency of 2.45 kHz and then plotted on amplitude versus time spectrograms as demonstrated with Figure 4-6 (bottom). The amplitude data was obtained by taking the fast-Fourier transform of the data and applying a low pass filter in order to eliminate high frequency "atmospherics" that are always present during data collection. After removing the high frequency noise components from the data, the inverse Fourier transform was performed. These atmospherics, or "spherics" for short, are strong impulses produced by strokes of lightning and are what typically initiate whistlers. Examples of spherics are seen as dark horizontal striping in Figure 4-5. In Figure 4-6, the frequency and amplitude information are shown along the same time-scale axis where the

large tick marks are one second apart. The center of the dark frequency band is at 2.45 kHz and the maximum width is approximately 200 Hz and the triggered emission falls approximately 600 Hz. The amplitude of the signal saturates at approximately -10 dB where -8 dB corresponds to 300 μ V/m. Saturation is a direct result of non-linear wave-particle interaction.

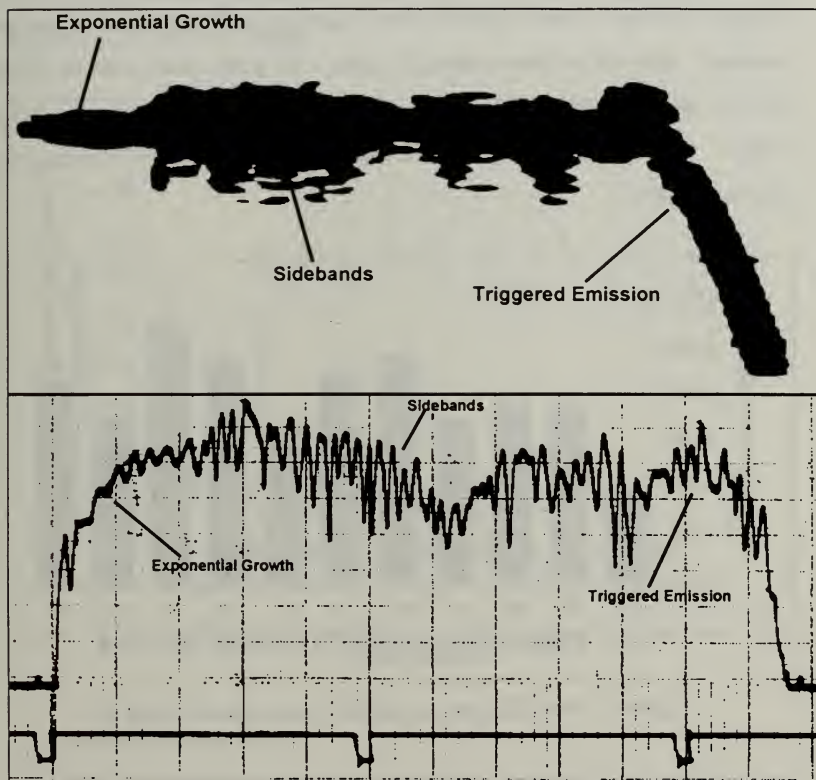


Figure 4-6. Example of Signal #5 (constant frequency and power) illustrating growth, saturation, sidebands and a triggered emission. Frequency vs. time (top) and Amplitude vs. time (bottom) are against the same time scale where the tick marks are one second apart.

1. Exponential Growth

As the VLF wave travels along a magnetic field line it may be amplified by counter streaming energetic electrons that spiral around the same field line. The details of this interaction are presented in the next chapter. The exponential growth rate for this example is 35 dB/sec and is typical of the signals seen during the ten hour period. The exponential growth continues until the signal saturates. Notice from Figure 4-6 that the frequency (top panel) remains relatively narrow during the initial growth period, and then broadens as sidebands are formed during saturation. The growth rates varied significantly over the ten hour period as demonstrated by Figure 4-7 which displays a 1.5 hour window. This figure demonstrates large changes in growth rate over a five minute time scale for Signal #5.

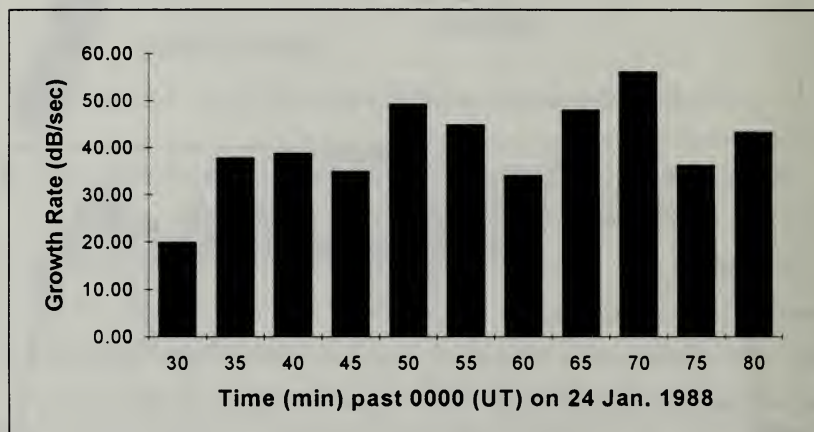


Figure 4-7. Plot of growth rate (dB/sec) versus time for Signal #5.

To investigate changes over a shorter time period, it is necessary to look at Signal #7 which was transmitted 24 seconds later. Figure 4-8 plots the ratio of Signal #7 growth rate to Signal #5. Signal #5 and Signal #7 were chosen as pairs because they are the most similar signals transmitted. This figure illustrates that the growth rates for these two

signals are the same within the uncertainty of the measurement given by the error bars. The average growth rate ratio was 0.95 ± 0.19 . It should also be noted that the growth rates were difficult to measure precisely and contain an average uncertainty of ± 5 dB/sec. From Table 3-2, Signal #5 was transmitted with a constant power level; however, Signal #7 was ramped in power at 10 dB/sec. Therefore, one may ask how can these two signals be compared if one has a transmitted power ramp in its profile? The answer to this will be discussed fully later in this chapter.

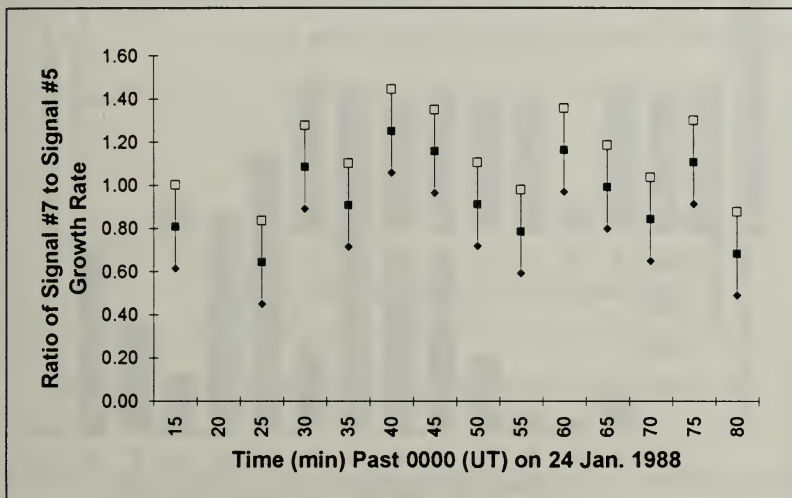


Figure 4-8. Ratio of Signal #7 (corrected) growth rate to Signal #5 growth rate during a 1.5 hour window.

2. Saturated Power Level

Typical to any system with negative feedback, an amplified signal reaches a steady-state power level. Therefore, this section will discuss some of the properties of the observed saturated levels and the next chapter will develop the wave-particle interaction and feedback mechanism in detail. Once again the saturated power level for Signal #5

varied significantly over a five minute time scale as illustrated by Figure 4-9. All of these saturation levels are normalized to what is thought to be the lowest unamplified power level during this 1.5 hour window. The calculation of the unamplified power level is not a trivial matter and will be explained fully later in this chapter. Note the normalized power levels, P_f/P_o in Figure 4-9 can also be thought of as gain levels,

$$G = \frac{P_f - P_o}{P_o} = \frac{P_f}{P_o} - 1 \quad (4.1)$$

where G is the signal gain, P_f and P_o are the final power and initial unamplified power level respectively. This is an excellent approximation when $P_f \gg P_o$.

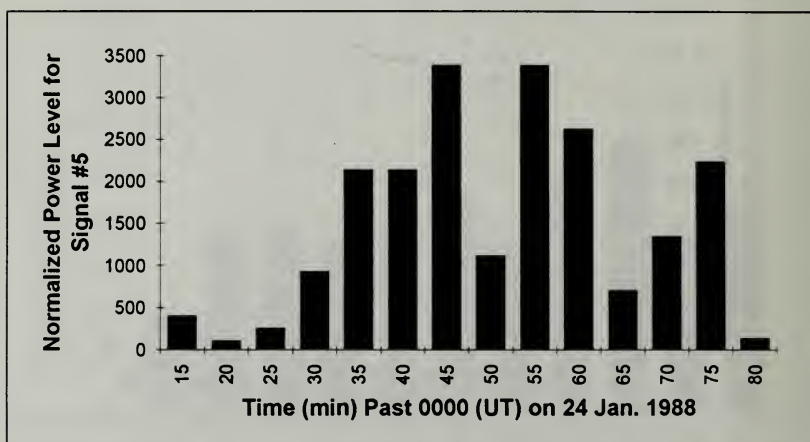


Figure 4-9. Chart of normalized power levels for Signal #5.

It is easy to see that gains as large as 35 dB are possible and that gains on the order of 30 dB occur frequently. Large gains like this are one of the main reasons these signals are studied. If the mechanism of this gain process can be fully understood, similar principles could be applied to free electron laser theory and design.

It is interesting to see how the saturated power levels change on the 30 second time scale. Just as was done for growth rate above, the ratio of the saturated power level for Signal #7 to that for Signal #5 is plotted in Figure 4-10.

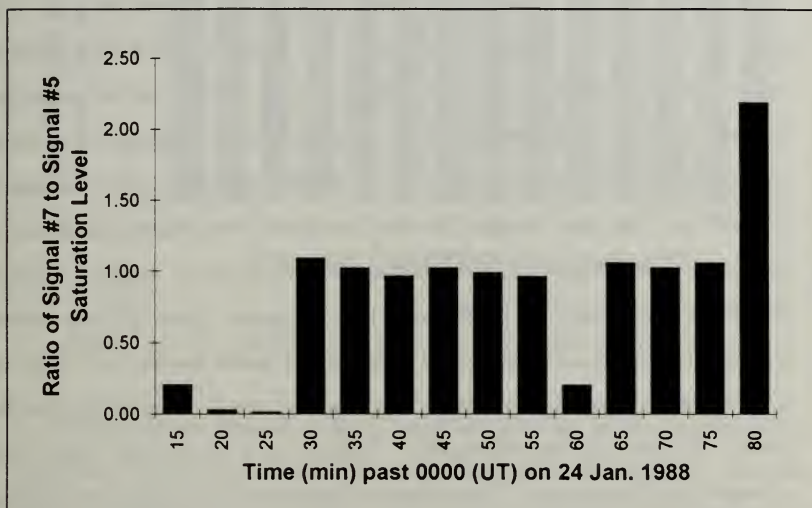


Figure 4-10. Chart of the ratio of saturated power level for Signal #7 to Signal #5.

When both signals reached a saturated level within the one minute transmission period, their signals levels are approximately equal, and thus the ratio is one. Using Chauvenet's criterion [Ref. 16] to reject outlying data in Figure 4-10, the average ratio was 1.02 ± 0.04 . When one of the signals did not grow to saturation for one reason or another, no correlation between Signal #5's and Signals #7's saturated signal level was observed, and the ratio was not constant nor predictable. In general both signals did saturate and on the 30 second time scale, their saturated signal levels are nearly equal. Estimating the time scale over which key experimental parameters change is useful in understanding the

mechanisms that cause the change. For this reason, the time scale question will continue to be emphasized throughout this chapter.

3. Sidebands

Sidebands produced during the ten hour period had the least variation of all of the experimental phenomena observed. Sidebands were only observed if the transmitted signal saturated, and were weakly observed in the fine structure of the subsequent triggered emission. During the saturated portion of the received signal, up to 8 harmonics of the sideband modulation were observed. The sideband frequencies were calculated by two methods. First, after the signal saturated, the up and down amplitude peaks, seen in the bottom panel of Figure 4-6, were counted and converted into a frequency. Second, the Δf was read directly off the frequency-time histograms. Both of these methods produced the same result within ± 5 Hz. However, the second method is far easier and more accurate because the amplitude variations are not simply sinusoidal because they contain all of the sideband information. Therefore, it is not obvious which peaks correspond to which sideband. The top panel of Figure 4-6 clearly illustrates the sideband broadening with $\Delta f \approx 25$ Hz. The reader may compare the results with the bottom panel of Figure 4-6. To illustrate the invariance of the sideband formation, Figure 4-11 plots the first sideband of Signal #5 versus time during a 1.5 hour window. The average modulation frequency for the first sideband of Signal #5 was 23.2 ± 1.8 Hz.

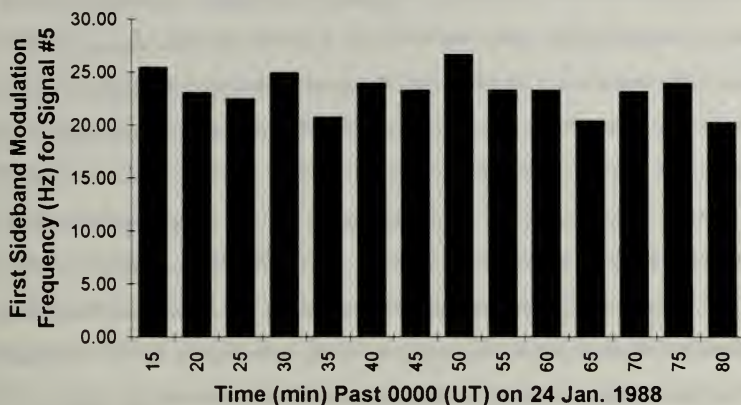


Figure 4-11. Plot of the first sideband frequency Δf versus time for Signal #5.

The formation of sidebands during an amplification process can be a complex subject. Sidebands are produced when the main carrier frequency is modulated by a secondary interaction process causing the signal to "beat." The modulation or beat frequency (Δf) can be many orders of magnitude less than the carrier frequency as is the case with the Siple experimental data as well as common FM radio signals. A clear cause for the sideband production in the Siple data is still under investigation. Possible explanations include (1) modulation by the transmitting antenna's peripheral equipment, (2) modulation by Canada's power line grid during reception, and (3) modulation caused by synchrotron oscillations due to strong field coupling of the counter-streaming electrons. The last possibility will be described in the next chapter and simulations will demonstrate good correlation with observed sideband frequencies.

4. Triggered Emissions

There are many different types of triggered emissions as already noted in Appendix A. During the ten hour observation period, over 90% of the triggered emissions were

"termination emissions." Termination emissions are triggered emissions that occur at the end of the transmitted pulse. Figure 4-6 is a good representative example of the type of termination emissions observed. When the signal is terminated, an emission is launched of equal signal strength that first rises in frequency then sharply drops in frequency. The rise in frequency is about 5% of the center frequency (2450 Hz); however, the drop in frequency is much larger and ranges between 20 to 50% of the center frequency. Once again no theory nor simulation has been able to describe triggered emission sweeps of 500 to 1200 Hz. Similarly, no theoretical mechanism has been formulated that explains why triggered emissions occur, and why they occur preferentially on the termination of a transmitted signal. One simple macroscopic explanation for the falling emission may be in terms of "phase-locked" hot electrons. Once the injected VLF wave train passes by the counter-streaming electrons, they are "forced" together in phase due to the influence of the wave. The electrons stay in phase as they approach the geomagnetic equator where the magnetic field, and therefore the gyro-frequency decreases. The electrons continue to radiate in proportion to the local gyro-frequency until they have lost sufficient energy to lose their phase-lock, or until they pass through the geomagnetic equator where the magnetic field strength gradient changes sign and disrupts the process. The process of electrons radiating coherently in the absence of an external electromagnetic field is called "super-radiance." There is a free electron laser (FEL) analog to this process which will be discussed in Chapter VII; however, the time scales are much different. For the Siple Station data, super-radiant coherency would have to be maintained for 0.2 to 0.5 seconds to explain the falling triggered emissions in all cases. But for FELs, it has been shown that electrons will only maintain their coherency in the absence of light for times on the order of nanoseconds.

It is easy to determine whether or not changes in the electrons' gyro-frequency are the same order of magnitude as the falling triggered emission sweeps. Consider electrons on the $L = 5.1$ magnetic field line as is the case for the Siple Station data, and suppose

some of the electrons stop interacting with the VLF wave 5° from the geomagnetic equator. At $L = 5.1$, they must travel 2.8×10^6 meters to reach the geomagnetic equator. For 1.5 keV electrons, this yields an average travel time of 0.33 seconds. During this time, their gyro-frequency changes by 232 Hz. These numbers fit nicely with the observed changes in frequency observed in the experimental data. It should be noted that these numbers are for illustration only and to show that triggered emission sweeps in the hundreds of Hertz are possible if they are connected to the hot electrons' gyro-frequency.

Another simple model for triggered emissions may lie in similar arguments that have been made to explain whistlers from lightning strokes. The termination of the transmitted signal is abrupt and impulsive; therefore, many Fourier components in frequency space are excited and contain significant energy. Since the medium is dispersive, the different frequency components travel at different group velocities. Moreover, each frequency "slice" of the triggered signal could find resonant hot electrons to amplify it. The net result of this process would be received signals at different frequencies at different delay times but with similar amplification.

5. Magnetospheric Events

Now that the ground work for most of the distinguishing characteristics of the received signals has been laid, it is important to reflect on the different types of events that occur in the magnetosphere that could cause the changes described in the last four sections. The three events that are considered important are the electron's bounce motion, the electron's drift motion, and electron injection events in and out of the magnetosphere. As already mentioned, the properties of the VLF waves change on the 5 minute and hour time scale, but do not change appreciably over the 30 second time scale.

From Figure 3-3, a typical bounce period for a 1.5 keV electron is about 5 seconds. This motion is too fast to be the cause of the changes described above. This means a typical hot electron bounces approximately 6 times between Signal #5 and Signal #7

transmission times. The typical drift period for the same electron is approximately 60 hours and the average drift velocity is 1000 m/sec. From satellite data [Ref. 17], the longitudinal extent for a typical duct is about 4° which corresponds to a duct radius of approximately 1.13×10^6 m at $L = 5.1$. Therefore, the electrons take about 19 minutes to leave the field aligned duct. These changes occur over time scales that are 4 times larger than the observed changes that happened during the 5 minute delay time between transmissions. Therefore, changes in the data are probably not due to bounce effects which occur too quickly and are not due to drift effects which occur too slowly.

The hot plasma effects that cause changes over the five minute time scale are not understood. The relevant physical parameters are: the input field intensity, resonant electron flux level or density, and the pitch angle anisotropy [Ref. 18]. Since the unamplified power levels of Signals #2a and #2b, illustrated in Figure 4-13, remain essentially constant, the VLF field input intensity may be assumed to be constant and the propagation conditions during that time period did not change. Therefore, the changes seen in the saturation levels of Signal #5 in Figure 4-9 are attributed to hot plasma effects. Following the work done by *Carlson et al.* [Ref. 18], the saturation levels and the growth rates are relatively insensitive to the pitch angle anisotropy. The pitch angle anisotropy is determined by a pitch angle distribution function. However, the saturation level, and to a lesser extent the growth rate, are strong functions of the hot electron flux level which determines the resonant electron population. Therefore, one possible explanation for the observed changes is that new sets of energetic electrons are injected into the duct during the five minute period. Injection events have a variety of time scales and are hard to classify. However, events occurring over five minutes are certainly not unreasonable. If the saturation level is indeed an indicator of the energetic electron density, then the Siple Station experimental method would be an excellent hot plasma diagnostic tool. Coupling the experimental data with computer simulation may actually lead to computing absolute hot electron densities in the magnetosphere.

C. THE THRESHOLD POWER CONCEPT

Throughout this chapter there have been some assumptions made about the initial unamplified signal level when calculating the normalized power (gain) and when comparing different signals that have different power profiles. This section will illustrate how the actual initial power level is determined, introduce the concept of a "threshold power level" and distinguish between spatial and temporal VLF wave growth.

1. Background

Early in the analysis of the data collected during the ten hour period on 23-24 Jan. 1988, received power levels were calculated. It was noticed that the left-hand polarized signals (Signals #2a and #2b) never achieved large gain levels nor did they demonstrate exponential growth. Electromagnetic waves that propagate parallel to the earth's magnetic field, B_0 , can either be right-hand circular polarized or left-hand circular polarized. [Ref. 19] The dispersion relationships for these two modes are given by [Ref. 19]

$$n^2 = \frac{c^2 k^2}{\omega^2} = 1 - \frac{\omega_p^2 / \omega^2}{1 - (\Omega/\omega)} \quad (\text{right-hand polarized}) \quad (4.2)$$

and

$$n^2 = \frac{c^2 k^2}{\omega^2} = 1 - \frac{\omega_p^2 / \omega^2}{1 + (\Omega/\omega)} \quad (\text{left-hand polarized}) \quad (4.3)$$

where n is the index of refraction, c is the speed of light, k is the wave number, ω is the VLF wave frequency, ω_p is the plasma frequency, and Ω is the electron gyro-frequency. These equations explain the propagation characteristics for each polarization direction. Figure 4-12 illustrates the range of frequencies over which each mode can propagate. If the wave frequency is less than the cutoff frequency, then the index of refraction is

negative and the left-hand polarized signal is attenuated and will not propagate. The left-hand cutoff frequency

$$\omega_L = \frac{-\Omega + \sqrt{\Omega^2 + 4\omega_p^2}}{2} \quad (4.4)$$

forms the first asymptote shown on Figure 4-12. Since most whistler and VLF signals traverse the magnetosphere where the wave frequency ω is less than or equal to $\Omega/2$, left-hand polarized signals are not observed. If the wave frequency is greater than ω_L , then a left-handed signal can propagate, but the frequency is too high to couple with the electrons responsible for wave amplification.

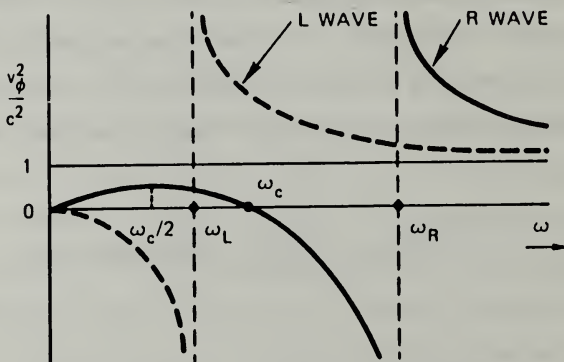


Figure 4-12. Plot of the squared normalized phase velocity versus frequency which clearly illustrates non propagation regions for both modes. [Ref. 19]

Figure 4-12 also displays a local maximum for the right-hand circularly polarized phase velocity occurs when $\omega = \Omega/2$. Recall from Chapter III, that this special condition, when

$\Lambda = 0.5$ or $\omega = \Omega/2$, determined the ducting ability and the density profile required for field-aligned propagation.

Since it has been determined that left-handed signals do not propagate in the frequency band of interest, why were signals received during the left-handed transmission time? To answer this question, one must understand the transmission properties of the VLF antenna and multiple duct excitation. Due to cutoff frequency calculations, which are described in the next section, the excited duct during this ten hour period was $L = 5.1$. The magnetic field aligned duct directly overhead at Siple Station is $L = 4.2$. This means that ducts at oblique angles were excited during transmission. Since the left-handed signals entered the ionosphere at oblique angles, the electric and magnetic fields can be represented by a signal that entered normal to the $L = 5.1$ duct, but consisted of left-handed and a right-handed components. The left-handed component was attenuated but the right-handed component continued to propagate and was received in Canada.

However, these signals which were initially left-handed did not show the typical characteristics of exponential growth, saturation and sidebands. In fact, these signals showed a flat amplitude profile slightly above the noise level. The amplitude levels during the hour and a half window are plotted in Figure 4-13. These signals were normalized to the same parameter as Signal #5 was in Figure 4-9; but, they are 350 (25 dB) times lower in amplitude and much more constant over this period.

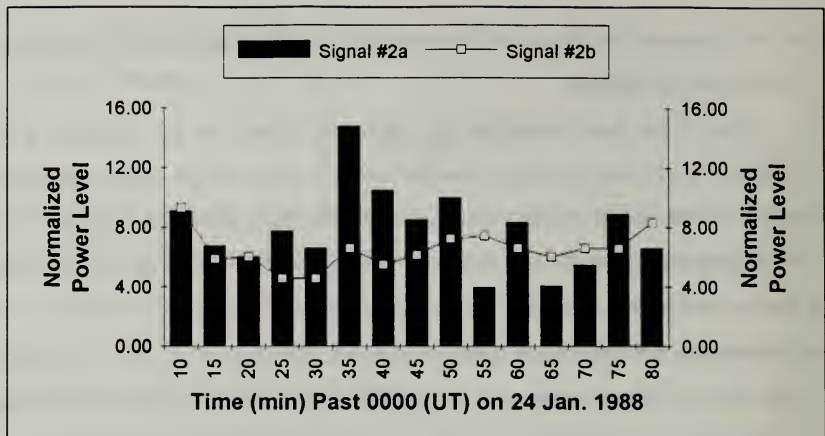


Figure 4-13. Plot of normalized power level versus time for Signal #2a (left-handed, constant transmitted power and frequency signal)

These signals were clearly unamplified, at least in the same sense as the rest of the signals. This led to the concept of a "threshold power level". A signal must be above the threshold power in order to demonstrate exponential growth. The threshold power can vary in time and depends on the local conditions in the interaction region. Since Signals #2a and #2b did not demonstrate exponential growth, it was determined that their levels never reached the threshold power.

2. Determining the Threshold Power

To test the threshold power concept, a suitable experiment with the existing data had to be devised. Signal #7, a two second long signal, was transmitted with a power ramp that started in the noise level seen in Figure 4-14, and was increased at 10 dB/sec up to full power during the first second, and then was held at full power during the next second. Therefore, the received amplified signal should demonstrate the following properties: (1) the initial power level is 10 dB below the initial power level for Signal #5 with, (2) the initial growth rate being equal to the transmitted power increase of 10 dB/sec until, (3) the

power level reaches the "threshold level" and begins to grow exponentially to saturation. This set of properties formulate a model that was applied to Signal #7's amplitude profile. There were only five times during the ten hour observation period that the atmospheric noise allowed Signal #7's first one second characteristics to be clearly seen. Figure 4-14 illustrates an example of applying the threshold model to an actual signal.

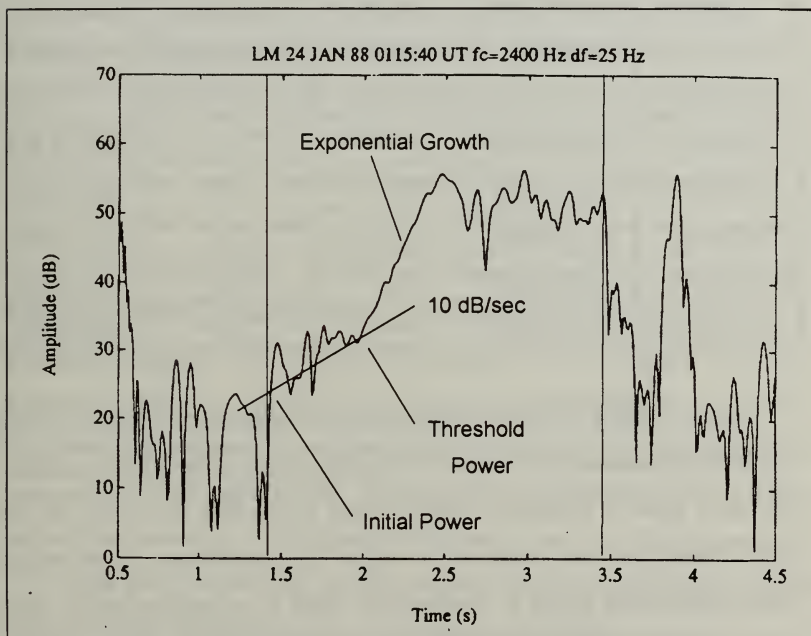


Figure 4-14. An example of Signal #7 at 0115 (UT) on 24 Jan. 1988 that demonstrates the initial 10 dB/sec growth, the threshold power, P_{th} , and the initial power, P_0 .

From Figure 4-14, the initial power, P_0 , the threshold power, P_{th} , and the initial 10 dB/sec growth rate are drawn in for clarity. The absolute scale of this figure is set by measurements made on other amplitude versus time charts where the relative signal strength was known. By making this comparison, 60 dB on Figure 4-14 corresponds to

300 μ V/m. Measurements like those on Figure 4-14 were made at a few other times as well. These results are presented in Table 4-1 below.

TABLE 4-1. COMPARISON BETWEEN SIGNAL #2a AND THE INITIAL AND THRESHOLD POWER LEVELS FOR A GIVEN TIME.

Time on 23-24 Jan. 1988	Initial Power Level (P_o) for Signal #7	Peak Power Level for Signal #2a	Threshold Power Level (P_{th}) for Signal #7	Initial Power Level (P_o) for Signal #5
0035 (UT)	13 (-35 dB)	15	51	180 (-24 dB)
0045 (UT)	2.1 (-43 dB)	8.5	14	28 (-32 dB)
0050 (UT)	6.5 (-38 dB)	10	23	68 (-28 dB)
0055 (UT)	1.0 (-48 dB)	4.0	5.6	3.6 (-40 dB)
0115 (UT)	8.7 (-37 dB)	8.9	22	89 (-27 dB)

Table 4-1 clearly shows that the peak power for Signal #2a falls between the initial and threshold power levels for Signal #7. All of the power levels have been normalized to the lowest measured initial power which occurred at time 0055 (UT). Also, the initial signal strength (shown in parenthesis) for Signal #7 is approximately 10 dB below the initial signal strength (shown in parenthesis) for Signal #5 as suggested earlier. Both of these observations confirm that the threshold power concept is valid. Moreover, by fitting the 10 dB/sec slope to the initial growth of Signal #7, a good estimate of its initial power level is made even though it is below the magnetospheric noise level. The threshold power phenomenon is a non-linear effect of the wave-particle interaction. Signal #5 is transmitted at full power from the beginning, and is therefore above the threshold power and begins exponential growth immediately as seen in Figure 4-6. All of the normalized power levels are relative to the lowest measurable initial power, P_o , of Signal #7. The

question about comparing the growth rate of Signal #7 to Signal #5 can now be answered. The slope measured for Signal #7 was done after it reached the threshold power and exponential growth had started. By this time, the 10 dB/sec transmitted power ramp was almost over.

3. Temporal and Spatial Wave Growth

Occasionally during a one minute time period the right-hand polarized signals did not display exponential growth nor did they reach a similar saturated power level. However, the signal would display some type of amplification and grow out of the ambient noise level. Therefore, it is convenient to describe two types of wave growth. In the typical situation, the signal enters a hypothetical interaction region which encompasses the VLF duct, and of course, the hot electron's gyro motion. The details of this region are spelled out clearly in the next chapter. When the wave enters this region and interacts strongly with the hot electrons, exponential growth occurs and is usually followed by saturation as illustrated in Figure 4-6. Since the interaction region is only a few percent of the total distance the electron can travel, this type of growth is called **temporal**. On the other hand, when the signals grew non-exponentially to some level barely out of the background noise level, it is called **spatial** growth. This term is chosen because the growth could have occurred anywhere along the ducted path the VLF wave traversed. This distance for the $L = 5.1$ field line is 12 earth radii. It should be noted that spatial growth and attenuation occurred for all of the signals whether or not temporal growth occurs.

4. A Sample Calculation

The Siple Station experimental data allows many physical parameters characteristic to the field aligned duct of interest to be computed. Signal #5 will be the signal of interest during this sample calculation. First of all, by knowing when the signal was transmitted, and when it was received, a delay time of 4 seconds was determined. Next, the signal cutoff frequency was determined by observing the frequency at which the ramped signals

were not received. Figure 4-15 illustrates the stability of the cutoff frequency during the ten hour period. Signal #4 was used to determine the cutoff frequency, since the highest frequency transmitted for this signal was 2.9 kHz. The scale on this figure is the same as that used in Figure 3-7. The cutoff frequency for this calculation is 2.42 ± 0.10 kHz. Due to the arguments made about ducted signals in Chapter III, the cutoff frequency is assumed to be half the equatorial gyro-frequency. This means the gyro-frequency at the geomagnetic equator for this field line is 4.84 kHz. A good thumb-rule is that the gyro-frequency for $L = 4$ is 13.65 kHz [Ref. 20]. Since the gyro-frequency is proportional to the magnetic field and the magnetic field at the geomagnetic equator is proportional to $1/L^3$ [Appendix B], the L -shell for this data is

$$L = 4 \left(\frac{13.65}{4.84} \right)^{\frac{1}{3}} = 5.6,$$

The actual L -shell was computed to be 5.1 by frequency dispersion analysis performed at Stanford University.

Now that the field line is known, the total distance traveled by the VLF wave can be computed by the equation given in Appendix B. The total arc length for $L = 5.1$ is $s = 7.68 \times 10^7$ m. Therefore, the average index of refraction over the path length is

$$\bar{n} = \frac{c \Delta t}{s} = \frac{(3.0 \times 10^8)(4)}{7.68 \times 10^7} = 15.6. \quad (4.5)$$

Assuming the dispersion relationship for the whistler propagation mode, the equatorial cold electron density can be computed.

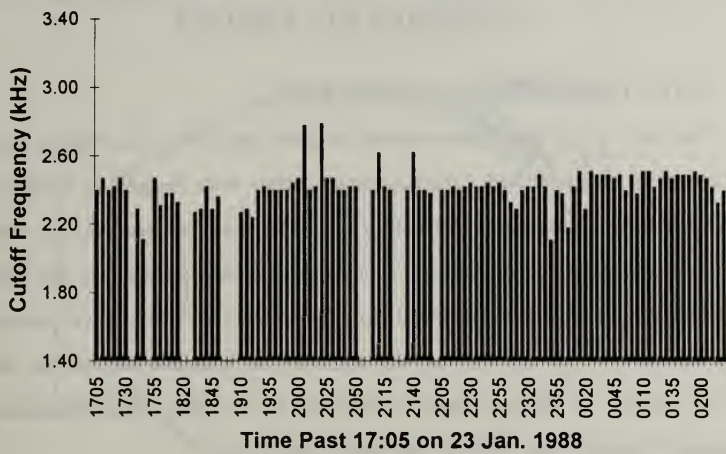


Figure 4-15. Plot of the cutoff frequency obtained using Signal #4 frequency ramp. The maximum transmitted frequency for Signal #4 was 2.90 kHz.

With this assumption, the average index of refraction can also be written as

$$\bar{n} = \int_{\text{wave path}} \left[\sqrt{1 + \frac{\omega_p^2(\lambda)}{\omega(\Omega(\lambda) - \omega)}} \right] \frac{d\lambda}{\lambda_o} = 15.6 \quad , \quad (4.6)$$

where λ is the geomagnetic latitude and λ_o is the latitude where the field line for $L = 5.1$ enters the earth. Notice the plasma frequency, ω_p , and the gyro-frequency, Ω , are functions of the geomagnetic latitude with their functional dependence given in Appendix B. After performing the integration, the equatorial cold electron density, ρ_c , is determined to be 71 electrons/cm³ and the equatorial index of refraction is 23. Both of these numbers are consistent with the description of the cold plasma given in Chapter III. The profiles for the cold electron density, gyro-frequency, and the plasma frequency are plotted in Appendix B.

V. WHISTLER AND VLF WAVE-PARTICLE INTERACTION THEORY

A. THE COLD BACKGROUND PLASMA

Until now, only a macroscopic view of the interaction between the VLF wave and the electrons has been described. The preceding chapters were intended to summarize the magnetospheric environment, terminology, general trends, and observations that have been made regarding the amplification of injected VLF wave signals. In this chapter, a mathematical model will be presented that describes the role of the cold background plasma, and the amplification of the VLF signals by the resonant electrons that make up the hot plasma. In the next chapter, this model is used in computer simulations that graphically illustrate several of the experimental observations.

The propagation of the VLF or whistler wave through the magnetosphere is affected by both the cold and hot plasma along its path. The cold plasma, as described in Chapter III, contains non-resonant electrons that determine the wave's dispersion relationship while the hot electrons amplify the wave [Ref. 21]. For now, the effects of the VLF wave will be ignored in order to determine the motion of the cold electrons. The cold electrons execute cyclotron motion around the earth's magnetic field lines as illustrated in Figure 3-2. The coordinate system for this model is shown in Figure 5-1 where the z -coordinate follows the VLF wave and is parallel to the propagation vector. This motion can be described by the Lorentz force equation where the position vector \vec{r} is given by

$$\vec{r} = \frac{V_{c\perp}}{\Omega} [-\cos(\Omega t + \theta), \sin(\Omega t + \theta), 0], \quad (5.1)$$

where $V_{c\perp}$ is the cold electron's perpendicular velocity, and $\Omega = eB/mc$ is the electron gyro-frequency. The radius of gyration is $r = V_{c\perp}/\Omega$, and θ is the electron's phase. Since the velocity of a hot electron is 30 to 50 times the velocity of the cold electrons, the small z velocity, of the cold electrons, is ignored. Also, the drift motion of a cold electron is so small that it too may be ignored.

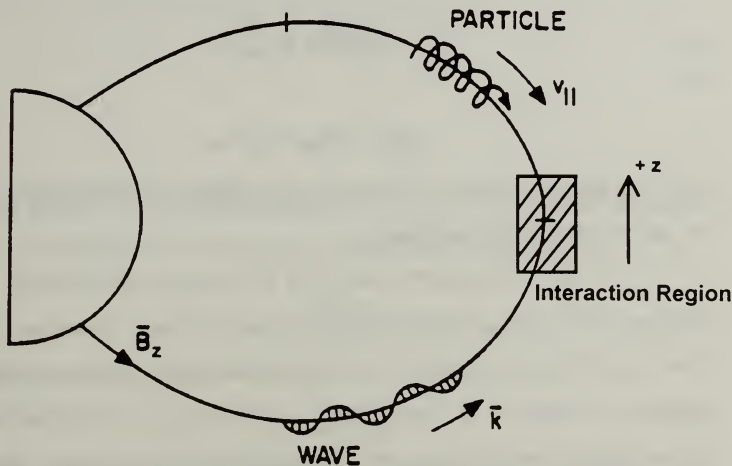


Figure 5-1. Schematic of the coordinate system used for the wave-particle interaction. The z-coordinate follows the magnetic field line and is parallel with the wave's propagation vector.

The cold electrons rotate in a clockwise fashion along the magnetic field line, and their velocity is equal to

$$\vec{V}_e = V_{e\perp} [\sin(\Omega t), \cos(\Omega t), 0]. \quad (5.2)$$

Once the VLF wave is included, the Lorentz force equation can be written as

$$\dot{\vec{V}}_e = -\frac{e}{m} \left[\vec{E}_w + \frac{\vec{V}_e}{c} \times (\vec{B}_w + \vec{B}) \right], \quad (5.3)$$

where \vec{E}_w and \vec{B}_w are the electric and magnetic field vectors of the propagating VLF, or whistler wave, and \vec{B} is the earth's geomagnetic field. Since the VLF wave's magnetic

field is so much smaller than the earth's magnetic field, it may be neglected in comparison for now. Equation 5.3 can be expanded into component form to yield

$$\dot{V}_{\alpha} + \Omega V_{\alpha} = -\frac{e}{m} E_{\alpha} , \quad (5.4)$$

and

$$\dot{V}_{\alpha} - \Omega V_{\alpha} = -\frac{e}{m} E_{\alpha} . \quad (5.5)$$

Since only right-hand circularly polarized waves propagate in the whistler mode (Figure 4-12), the VLF fields can be expressed by

$$\bar{E}_w = E_w(t)[\cos(\Psi), -\sin(\Psi), 0], \quad \bar{B}_w = B_w(t)[\sin(\Psi), \cos(\Psi), 0] . \quad (5.6)$$

The phase of the propagating wave is $\Psi(t) = kz - \omega t + \phi(t)$ where k is the wave number, ω is the wave frequency, and $\phi(t)$ is the time-dependent phase. Since the wave and the electrons are coupled by the Lorentz force equations above, the electrons' steady-state motion must have the same space and time dependence as the VLF wave. Therefore, the cold electrons' motion may be described by

$$\bar{V}_c = V_{c\perp}[\sin(\Psi), \cos(\Psi), 0] , \quad (5.7)$$

which is then used in (5.4) or (5.5) and requires

$$V_{c\perp} = -\frac{eE_w}{m(\Omega - \omega)} , \quad (5.8)$$

for steady-state.

The current density generated by the motion of the cold electrons in the magnetosphere can be written as

$$\bar{J}_c = -e\rho_c \bar{V}_c = \frac{e^2 \rho_c E_w}{m(\Omega - \omega)} [\sin(\Psi), \cos(\Psi), 0] , \quad (5.9)$$

where ρ_c is the cold electron density. [Ref. 22]

Now there is sufficient information to solve for the dispersion relationship due to the cold plasma. This current density and the expressions for the VLF wave's electric and

magnetic fields from Equation (5.6), may be used to solve Ampere's Law and Faraday's Law to yield

$$\bar{\nabla} \times \bar{B}_w = \frac{4\pi}{c} \bar{J}_c + \frac{1}{c} \frac{\partial \bar{E}_w}{\partial t} , \quad (5.10)$$

and

$$\bar{\nabla} \times \bar{E}_w = -\frac{1}{c} \frac{\partial \bar{B}_w}{\partial t} . \quad (5.11)$$

Assuming that the VLF envelope parameters E_w , B_w , and ϕ are constant with time and space (i.e. no amplification or attenuation), then Ampere's Law simplifies to

$$B_w c k = \frac{4\pi e^2 \rho_c E_w}{m(\Omega - \omega)} + E_w \omega , \quad (5.12)$$

and Faraday's Law reduces to

$$E_w c k = B_w \omega . \quad (5.13)$$

By definition, the index of refraction is $n = ck/\omega$. Therefore, (5.13) reduces to $B_w = nE_w$. Substituting this relationship into (5.12) yields the well-known dispersion relation for right-hand polarized VLF waves in a magnetized plasma,

$$n^2 = \frac{c^2 k^2}{\omega^2} = 1 + \frac{\omega_p^2}{\omega(\Omega - \omega)} . \quad (5.14)$$

This equation was also seen in (4.2) during the explanation of whistler mode wave propagation in Chapter IV. The plasma frequency, ω_p , is given by

$$\omega_p^2 = \frac{4\pi e^2 \rho_c}{m} . \quad (5.15)$$

Typically for VLF and whistler signals, $\omega_p \gg \omega$, and $\omega_p \gg \Omega$, then (5.14) reduces to

$$n \approx \frac{\omega_p}{\sqrt{\omega(\Omega - \omega)}} . \quad (5.16)$$

B. THE WAVE EQUATION

The total current in the interaction region consists of both the hot and cold electrons. In order to develop a wave equation that describes the evolution of the VLF wave envelope, the total current, $\bar{J} = \bar{J}_c + \bar{J}_h$, must be used. The hot electron current for a single electron is

$$\bar{J}_h = -eV_{h\perp}[-\sin(\Theta), \cos(\Theta), 0], \quad (5.17)$$

where $V_{h\perp}$ is the transverse velocity of a hot electron, and $\Theta = \Omega t + \theta$ is the phase of the electron cyclotron motion. In this development, it is assumed that the variation of the VLF wave envelope in time and space will be small over on wavelength so that

$$\dot{E}_w \ll \omega E_w, \quad \dot{\phi} \ll \omega \phi, \quad E'_w \ll kE_w, \quad \phi' \ll k\phi. \quad (5.18)$$

This slowly-varying amplitude and phase approximation is valid when the VLF envelope describes a narrow-band VLF wave [Ref. 23]. Using the right-hand polarized waves of (5.6), Ampere's Law can be projected onto two unit vectors,

$$\hat{\epsilon}_1 = [\sin(\Psi), \cos(\Psi), 0], \quad \hat{\epsilon}_2 = [\cos(\Psi), -\sin(\Psi), 0], \quad (5.19)$$

to yield two scalar first-order differential equations,

$$ckB_w - \omega E_w + cB_w \partial_z \phi + E_w \partial_t \phi = \frac{\omega_p^2 E_w}{\Omega - \omega} - 4\pi e V_{h\perp} \cos(\Psi + \Theta), \quad (5.20)$$

and

$$c\partial_z B_w + \partial_t E_w = -4\pi V_{h\perp} \sin(\Psi + \Theta), \quad (5.21)$$

where $\partial_z(..) = \partial(..)/\partial z$ and $\partial_t(..) = \partial(..)/\partial t$. Using (5.12) and (5.13), these equations simplify to

$$ncB_w \partial_z \phi + B_w \partial_t \phi = -4\pi en V_{h\perp} \cos(\Psi + \Theta), \quad (5.22)$$

and

$$nc\partial_z B_w + \partial_t B_w = -4\pi en \sin(\Psi + \Theta). \quad (5.23)$$

It is convenient to define a quantity b :

$$b = \frac{eB_w}{mc} \exp(i\phi). \quad (5.24)$$

The complex field b has units of inverse seconds (s^{-1}), and is $\approx 1s^{-1}$ when the VLF wave amplitude is at the largest expected value of 10 pT. By defining and taking the partial derivatives of b with respect to z and t , Equations (5.22) and (5.23) can be reduced to

$$(nc\partial_z + \partial_t)b = -\frac{i4\pi e^2}{m}V \exp(-i(\zeta + \Theta)) , \quad (5.25)$$

where $\zeta = kz - \omega t + \int_0^t \Omega(t')dt'$ is the longitudinal electron phase, and $V = nV_{h\perp}/c$ is the dimensionless transverse electron velocity. The longitudinal phase reduces to $\zeta = kz - \omega t + \Omega_0 t$ for a homogeneous geomagnetic field.

Since the current in Ampere's Law is for a single electron in the hot plasma, the current for a beam of electrons is obtained by averaging over the longitudinal phase ζ , the transverse velocity V , and the transverse electron phase Θ . This average is done over all the electrons in a differential element of volume at a local space-time point so that the hot electron density is a weighting factor. Therefore, the wave equation (5.25) reduces to

$$(nc\partial_z + \partial_t)b = -i\omega_h^2 \langle V \exp(-i(\zeta + \Theta)) \rangle , \quad (5.26)$$

where $\omega_h^2 = 4\pi e^2 p_h / m$ is the hot electron plasma frequency and $\langle \dots \rangle$ symbolically denotes the average over all sampled electrons. Assuming the VLF wave envelope is spatially flat over many wavelengths, the $\partial_z b$ term is \approx zero, and the wave equation reduces to

$$\dot{b} = -i\omega_h^2 \langle V \exp(-i(\zeta + \Theta)) \rangle . \quad (5.27)$$

The incoming wave enters the interaction region, and meets a random distribution of hot electrons. The electrons are random in velocity and phase, and are initially governed by a distribution function. By studying (5.27), it is easy to see that the averaging process will initially cause the average $\langle \dots \rangle$ to be small, and the VLF field b would not be amplified. This disagrees with experimental observations made in the previous chapters where gains as large as 35 dB were demonstrated in Figure 4-9. Therefore, to obtain a non zero average, the hot electrons' transverse velocity, longitudinal and transverse phases must evolve in time. These dynamical variables are determined by the hot electrons' equations of motion.

C. THE HOT ELECTRON EQUATIONS OF MOTION

The motion of the hot electrons, like the cold, is governed by the Lorentz force equation

$$\dot{\vec{V}}_h = -\frac{e}{m} [\vec{E}_w + \vec{V}_h \times (\vec{B}_w + \vec{B})] , \quad (5.28)$$

but the magnetic field of the VLF wave cannot be dropped as was the case for the cold electrons. The geomagnetic field is of the form $\vec{B} = [0, 0, B(z)]$ in accordance with Figure (5-1). The equations of motion can then be written as [Ref. 24]

$$\dot{V}_x = -\frac{e}{m} [E_x + \frac{1}{c} (V_y B_z - V_z B_y)] + \frac{V_x V_z}{2B_o} \partial_z B_z , \quad (5.29)$$

$$\dot{V}_y = -\frac{e}{m} [E_y + \frac{1}{c} (V_z B_x - V_x B_z)] + \frac{V_y V_z}{2B_o} \partial_z B_z , \quad (5.30)$$

$$\dot{V}_z = -\frac{e}{mc} [V_x B_y - V_y B_x] - \frac{(V_x^2 + V_y^2)}{2B_o} \partial_z B_z , \quad (5.31)$$

where the second term on each equation describes the motion of an electron in a general non-uniform magnetic field. Equations (5.29), (5.30), and (5.31) are known as the inhomogeneous equations of motion, since the earth's non-uniform magnetic field can be taken into account. It is assumed that the earth's dipole magnetic field within the interaction region near the geomagnetic equator can be approximated by [Ref. 24]

$$B(z) \approx B_o \left(1 + \frac{9z^2}{2R_e^2 L^2} \right) = B_o (1 + qz^2) , \quad (5.32)$$

where $q = 9 / (2R_e^2 L^2)$, R_e is the earth's radius (6370 km) and B_o is the geomagnetic field strength at the equator. Substituting the transverse electric and magnetic fields, Equation (5.6), and the longitudinal magnetic field, $B(z)$, into the equations of motion yields

$$\dot{V}_x = -\frac{e}{m} \left(E_w \cos(\Psi) + \frac{V_y}{c} B_z - \frac{V_z}{c} n E_w \cos(\Psi) \right) + V_x V_z qz , \quad (5.33)$$

$$\dot{V}_y = -\frac{e}{m} \left(-E_w \sin(\Psi) + \frac{V_z}{c} n E_w \sin(\Psi) - \frac{V_x}{c} B_z \right) + V_y V_z qz , \quad (5.34)$$

$$\dot{V}_z = -\frac{e}{m} \left(\frac{V_x}{c} n E_w \cos(\Psi) - \frac{V_y}{c} n E_w \sin(\Psi) \right) - (V_{x_0}^2 + V_{y_0}^2) qz . \quad (5.35)$$

The transverse velocity components can be written as

$$V_x = -V_{h\perp} \sin(\Theta) , \quad V_y = V_{h\perp} \cos(\Theta) . \quad (5.36)$$

Substituting the transverse velocity components into Equation (5.35) yields [Ref. 24]

$$\dot{V}_z = \frac{e n V_{h\perp} E_w}{m} \sin(\Psi + \Theta) - V_{h\perp}^2 qz . \quad (5.37)$$

Taking the time derivatives of the transverse velocity components, (5.36) and substituting them into (5.33) and (5.34) yields new transverse equations of motion [Ref. 24]

$$\dot{V}_{h\perp} = \frac{e E_w}{m} \left(1 - \frac{n V_z}{c} \right) \sin(\Psi + \Theta) + V_z V_{h\perp} qz , \quad (5.38)$$

and

$$\dot{\Theta} = \frac{e E_w}{m V_{h\perp}} \left(1 - \frac{n V_z}{c} \right) + \frac{e B(z)}{mc} . \quad (5.39)$$

Now that the inhomogeneous equations of motion have been developed, it is useful to place them into a form that is more convenient for computer simulations. Using these relationships, and the magnitude of the wave field parameter, $|b| = e n E_w / mc$, the equations of motion become

$$\dot{V}_z = |b| V_{h\perp} \sin(\Psi + \Theta) - V_{h\perp}^2 qz , \quad (5.40)$$

$$\dot{V}_{h\perp} = \frac{c |b|}{n} \left(1 - \frac{n V_z}{c} \right) \sin(\Psi + \Theta) + V_z V_{h\perp} qz , \quad (5.41)$$

$$\dot{\Theta} = \frac{c |b|}{n V_{h\perp}} \left(1 - \frac{n V_z}{c} \right) \cos(\Psi + \Theta) + \Omega_o (1 + qz^2) , \quad (5.42)$$

where $\Omega_o = e B(0) / mc$ is the hot electron gyro-frequency at the geomagnetic equator.

At this point of the derivation, it is convenient to solve for the motion of the electrons in the earth's dipole field in the absence of the VLF wave and assume the influence of the

VLF wave is a microscopic perturbation to the macroscopic dipole motion. From Ref. 24, the z -motion in the earth's dipole magnetic field is described by

$$\ddot{z} = -\frac{V_{\perp o}^2}{2B_o} \partial_z B(z) . \quad (5.43)$$

Using the dipole approximation, (5.32), the z -motion reduces to $\ddot{z} = -V_{\perp o}^2 qz$, which can be solved exactly to yield

$$z(t) = \frac{V_{\perp o}}{\omega_m} \sin(\omega_m t) , \quad (5.44)$$

where $\omega_m^2 = V_{\perp o}^2 q$ is the "mirror frequency" and is equal to $\approx 1 \text{ s}^{-1}$ for a 1.5 keV electron, at $L = 5.1$ and a 45° pitch angle. Since the time the electrons spend in the interaction region is typically small compared to the bounce period, the small angle approximation is valid. Therefore, the z -motion is approximately given by

$$z \approx V_{\perp o} t , \quad (5.45)$$

for the terms that describe the motion in the dipole field.

According to experimental observation, most whistler activity and VLF wave amplification occurs when $\omega/\Omega = 0.5$ as described in Chapter III. This situation is known as the "ducted cutoff condition" because a wave cannot stay in the same duct once this transition is crossed. When the assumption is made that the VLF frequency, at the geomagnetic equator, is at the ducted cutoff frequency, $\omega = \Omega_o/2$, some nice properties for the electrons and wave arise. The phase and group velocity are given by

$$V_p = \frac{c}{n} = \frac{\omega}{k} , \quad V_g = \frac{d\omega}{dk} . \quad (5.46)$$

The group velocity can be evaluated in terms of the index of refraction, n , using (5.16) to yield

$$V_g \approx 2 \frac{c}{n} \left(1 - \frac{\omega}{\Omega} \right) . \quad (5.47)$$

Using the ducted cutoff frequency approximation, the group velocity, at the geomagnetic equator, reduces further to

$$V_{g_o} \approx \frac{c}{n} \approx V_{p_o} . \quad (5.48)$$

Therefore, the group and phase velocities are approximately equal at this special frequency where the majority of wave amplification occurs. Resonance is defined when $v = 0$ or $kV_z = \omega - \Omega$. Therefore, when the electrons are resonant at the geomagnetic equator with the VLF wave at the ducted cutoff frequency, $V_{z_o} \approx -c/n = -\omega/k \approx -V_{p_o}$, so that the electrons and the wave are traveling at equal speeds in opposite directions. [Ref. 25] Substituting these approximations into the equations of motion yield

$$\dot{V}_z = |b|V_{h\perp} \sin(\Psi + \Theta) - \frac{V_{h\perp}^2 q\omega t}{k} , \quad (5.49)$$

$$\dot{V}_{h\perp} = \frac{2c|b|}{n} \sin(\Psi + \Theta) + \frac{V_{h\perp} q\omega^2 t}{k^2} , \quad (5.50)$$

$$\dot{\Theta} = \frac{2c|b|}{nV_{h\perp}} \cos(\Psi + \Theta) + \Omega(t) , \quad (5.51)$$

where the gyro-frequency is now given by

$$\Omega(t) \approx \Omega_o \left(1 + \frac{q\omega^2 t^2}{k^2} \right) . \quad (5.52)$$

The second term in (5.51) causes Θ to evolve rapidly, which shows up as a quickly evolving phase in all three equations of motion. But, writing

$$\Theta = \theta(t) + \int_0^t \Omega(t') dt' , \quad (5.53)$$

allows us to follow the fast part of the electron motion along the field line, with $\int_0^t \Omega(t') dt'$, and use $\theta(t)$ for the slow evolution caused by the VLF wave.

The argument inside the sinusoidal functions can be rewritten in terms of the new variables,

$$\Psi + \Theta = kz - \omega t + \int_0^t \Omega(t') dt' + \theta + \phi = \zeta + \theta + \phi , \quad (5.54)$$

where ζ is the longitudinal electron phase defined earlier. Using the definition of the electron phase, the electron phase velocity becomes

$$v = \dot{\zeta} = kV_z - \omega + \Omega(t) = kV_z + \omega + \frac{2q\omega^3 t^2}{k^2} , \quad (5.55)$$

and the electron phase acceleration becomes

$$\dot{v} = \ddot{\zeta} = k\dot{V}_z + \dot{\Omega}(t) = k\dot{V}_z + \frac{4q\omega^3 t}{k^2} . \quad (5.56)$$

Substituting (5.40) into (5.56) and recalling the definition of the normalized transverse velocity, $V = nV_{h\perp}/c$, and the wave number, $k = n\omega/c$, the inhomogeneous equations of motion become

$$\dot{v} = \ddot{\zeta} = \omega V |b| \sin(\zeta + \theta + \phi) + \frac{q\omega^3}{k^2} (4 - V_o^2) t , \quad (5.57)$$

$$\dot{V} = 2|b| \sin(\zeta + \theta + \phi) + \frac{V q \omega^2 t}{k^2} , \quad (5.58)$$

$$\dot{\theta} = \frac{2|b|}{V} \cos(\zeta + \theta + \phi) . \quad (5.59)$$

These equations describe the motion of a hot electron interacting with a single VLF wave mode. The second term in (5.57) gives rise to an interesting result. When $V_o = 2$, the second term in (5.57) is zero for all time, t , and the effect of the inhomogeneous magnetic field on the electron's phase acceleration is minimized. Because (5.57) and (5.58) are coupled, the inhomogeneous field still plays a role in the evolution of v . However, since (5.58) contains the factor, $\omega \approx 10^4/s$, to one less order than (5.57), the transverse velocity evolves much more slowly than v in the interaction region. Therefore, the phase velocity for electrons with $V_o = 2$, evolve as though they are in a homogeneous magnetic field. This result can be explained by looking at (5.55). As an electron moves away from the geomagnetic equator, its parallel velocity decreases, but its gyro-frequency increases. Therefore, these effects compete with each other, unless the initial dimensionless perpendicular velocity equals two, and then they cancel each other.

D. TAPER AND THE PENDULUM EQUATION

1. Taper

Free electron lasers (FELs) use a technique called "tapering" where the undulator parameter, K , is decreased by reducing the magnetic field strength. This allows the electrons to remain resonant and coupled to the light longer as energy is extracted from them. Tapering is performed only on one end of the undulator and therefore, it is not longitudinally symmetric. By placing the equations of motion for an electron in the magnetosphere in an analogous form to an electron in a tapered FEL, insight of the effects of the inhomogeneous magnetic field can be obtained. Since the electrons in the magnetosphere travel in a dipole magnetic field, they are subjected to a symmetric taper about the geomagnetic equator. The taper parameter, δ , is defined as

$$\delta = \frac{\omega^2 q}{k^2} = \frac{c^2 q}{n^2} = \frac{9c^2}{2n^2 R_e^2 L^2} . \quad (5.60)$$

Substituting the taper parameter definition into the equations of motion yields

$$\ddot{\zeta} = \omega V |b| \sin(\zeta + \theta + \phi) + \omega \delta (4 - V_o^2) t , \quad (5.61)$$

$$\dot{V} = 2|b| \sin(\zeta + \theta + \phi) + V \delta t , \quad (5.62)$$

$$\dot{\theta} = 2 \frac{|b|}{V} \cos(\zeta + \theta + \phi) . \quad (5.63)$$

The taper parameter, δ , has a typical value of 0.43 s^{-2} for the experimental data shown in Chapter IV where $n \approx 30$ and $L = 5.1$. Tapered free electron lasers have an equation similar to (5.61); however, the tapered term in the equation is a constant with no time dependence.

2. The Pendulum Equation

In certain situations, the equations of motion may be reduced by neglecting the effects of the tapered magnetic field. If the index of refraction is large and the L -shell is also large, then δ is small and the taper terms may be dropped. Also, if the interaction region is

small, then the earth's magnetic field does not vary appreciably within it. In this case, the interaction time, t , is short and the taper terms may be dropped. Finally, the equations of motion may be imported to a special interaction region where the magnetic field does not vary. In this situation, the taper terms could have been appropriately removed from the beginning since B_z is constant and $\delta = 0$. Under these restrictions, the equations of motion become

$$\dot{\zeta} = \ddot{\zeta} = \omega V |b| \sin(\zeta + \theta + \phi) , \quad (5.64)$$

$$\dot{V} = 2|b| \sin(\zeta + \theta + \phi) , \quad (5.65)$$

$$\dot{\theta} = 2 \frac{|b|}{V} \cos(\zeta + \theta + \phi) . \quad (5.66)$$

At this point, Equation (5.64) can be identified as the pendulum equation describing the nonlinear longitudinal motion of the hot electrons. A similar pendulum equation for the free electron laser was developed many years ago. [Ref. 26] Without the effects of the tapered magnetic field, the transverse motion of the electrons, described by (5.65) and (5.66), evolve much more slowly since they do not contain the factor $\omega \approx 10^4/\text{s}$ in them.

VI. SIMULATIONS AND DISCUSSION

A. SOLVING THE HOMOGENEOUS EQUATIONS OF MOTION

The equations of motion developed in Chapter V are coupled, non-linear, first-order differential equations. Therefore, the only method of solution is through the use of numerical techniques. Many of the observed effects, seen in the experimental data, can be simulated by assuming the geomagnetic field in the interaction region is uniform. Therefore, the equations of motion simplify to Equations (5.64), (5.65), and (5.66). Using these equations, $v = \dot{\zeta}$, and the wave equation (5.27), the self-consistent motion of each electron can be solved numerically for a single VLF wave mode. By assuming a finite time-step size, Δt , these equations are solved using the Euler-Cromer method of integration. During these simulations, a section of the electron stream that is one VLF wavelength long is followed through the interaction region where it can interact. Since the length of the electron stream section is much shorter than the train of counter-propagating VLF waves, end effects of the interaction can be ignored and only a single VLF mode considered.

In order to represent $\approx 10^{13}$ electrons contained within the interaction region one wavelength long, a few (≈ 1000) sample electrons are spread uniformly in the initial phases ζ_0 and θ_0 ranging between $-\pi$ and π . The initial values for the longitudinal phase velocity v_0 are determined by the distribution function $f(v_0)$, while $g(V_0)$ is the initial distribution of the dimensionless transverse velocity V_0 . Since the equation of motion for $\dot{\Theta}$ involves V^4 , it is imperative that $g(V_0)$ go to zero for small V . Indeed, electrons with small pitch angles are precipitated out of the magnetosphere instead of mirroring as was discussed in Chapter III. The real and imaginary parts of the initial VLF field are taken to be $b_r = b_0$ and $b_i = 0$, so that the initial VLF phase is $\phi_0 = 0$ [Ref. 25]. The hot plasma frequency can range between 1 to 100s^{-1} in the region of interest [Ref. 10]. The interaction time, T , is defined as the time an electron is in the field of the VLF wave, which is typically less than

one second. During this time, resonant electrons travel about $cT/n \approx 10^4$ km $\approx 1.6 R_e$ [Ref. 21].

1. Weak VLF Fields and Low Gain

In a homogeneous geomagnetic field, the whistler-mode wave-particle interaction can be divided into regimes similar to a free electron laser (FEL). The simplest case to examine is a mono-energetic beam where $f(v) = \delta(v - v_o)$ and $g(V) = \delta(V_o - 1)$ corresponding to a pitch angle of 45° . The VLF wave frequency is taken to be 2450 Hz with an interaction time of $T = 1$ s. A weak VLF field is identified, in an analogous manner to a FEL, by $|b| \leq \pi / \omega T^2 = 2 \times 10^{-4} s^{-1}$ [Ref. 25]. Low gain occurs when $\omega \omega_h^2 T^3 \leq \pi$, or when $\omega_h \leq \sqrt{\pi / \omega T^3} = 0.014 s^{-1}$, similar to a FEL [Ref. 25]. Figure 6-1 is a simulation of a weak VLF field and low gain. In this figure, the plot on the left shows the electron phase velocity, v , versus the electron phase, ζ . In the phase-space plot, 20 electrons out of 1000 used, are plotted with the path and the final positions shown. Those paths that move down in v indicate that the energy is given up by the electrons to the wave, while those moving up in v are removing energy from the wave. In this case, the electrons move up almost as much as they move down, so the net transfer of energy is small. Also, the electrons clearly bunch around two values of ζ in one wavelength of the VLF wave because (5.59) contains two phase terms, ζ and θ , that initially range between $\pm\pi$ uniformly. The right-hand plots show how the VLF wave power (in dB) and phase, ϕ , develop over the course of the interaction. The gain is a measure of the amount the VLF wave field intensity changes over the interaction time and is defined, as before, as

$$G = \frac{|b(t)|^2}{|b(0)|^2} - 1 = \frac{P(t)}{P(0)} - 1 . \quad (4.1)$$

In this regime, the maximum low gain in weak fields can be expressed analytically as

$$G \approx 0.135 \omega \omega_h^2 (T - t_b)^3 \approx 0.21 \text{ dB} , \quad (6.1)$$

where $t_b \approx (2/\omega\omega_h^2)^{1/3} \approx 0.5s$, is the bunch time of the electrons seen in Figure 6-1 [Ref. 25]. This is close to the gain computed in the simulation of 0.23 dB. There is also a small phase advance in the VLF wave given by $\Delta\phi \approx \omega\omega_h^2 T^3 / 12$ [Ref. 25]. The phase only advances a small amount, ≈ 0.25 radians, during the interaction. In this simulation, the VLF field starts out weak and stays weak because the hot plasma frequency is small. This is required for low gain, since the VLF field is driven by a term proportional to ω_h^2 . The electrons stay in closed phase-space orbits as indicated by the gray lines drawn at [Ref. 25]

$$\Delta v = \pm 2\sqrt{|b_{final}| \omega} . \quad (6.2)$$

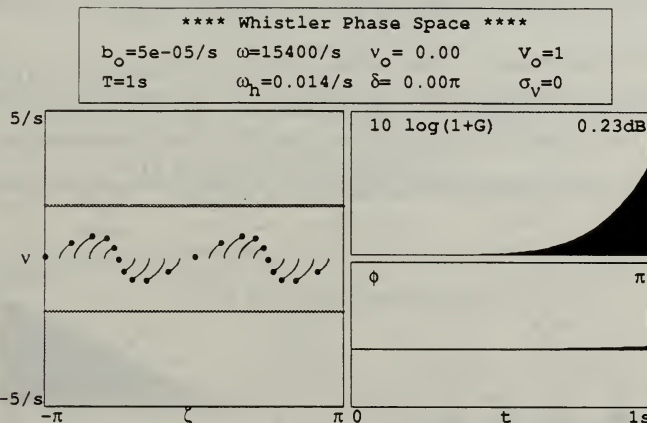


Figure 6-1. Electron phase-space, VLF wave power and phase for weak fields and low gain.

2. Weak VLF Fields and High Gain

For larger and more realistic hot plasma frequencies, it is easy to cross into the regime of high gain because of the ω_h^2 dependence. Figure 6-2 demonstrates a simulation with the same parameters as Figure 6-1 except that the hot plasma frequency was increased by a factor of ten to 0.14/s which is greater than the threshold for high gain described above. The electrons still bunch around two points as before, except now, the electrons with

decreasing phase velocity fall further than the electrons with increasing phase velocity. Therefore, the net result is a large amount of energy is given up to the VLF wave. Also, the wave's phase advances significantly during the interaction so that the points around which the electrons bunch are displaced slightly along ζ . Even though the VLF wave starts out small, the larger driving current increases the amplitude of the VLF wave and the gain. The VLF wave's power increases exponentially with time and reaches a final value of 30 dB. In the high gain regime, the final value of G can be expressed analytically as [Ref. 25]

$$G \approx \exp\left[\left(\omega\omega_h^2/2\right)^{1/3}\sqrt{3T}\right]/9 \approx 30 \text{ dB} , \quad (6.3)$$

while the phase change is a linear advance given by $\Delta\phi \approx (\omega\omega_h^2/2)^{1/3}T/2 \approx 2.7$. Also, the characteristic bunching time can be expressed as $t_b \approx (2/\omega\omega_h^2)^{1/3} \approx 0.19 \text{ s}$.

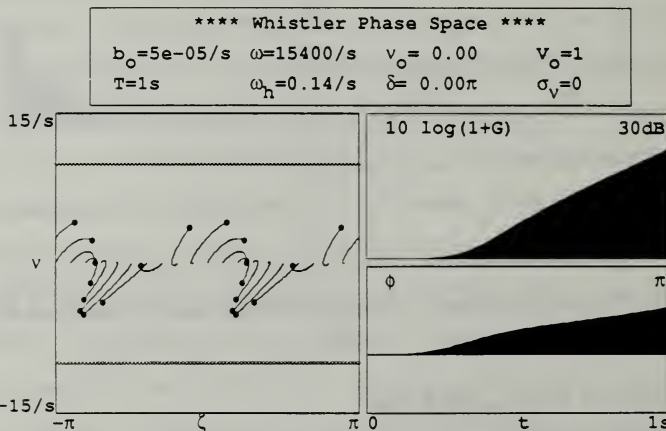


Figure 6-2. Electron phase-space, VLF wave power and phase for weak fields and high gain.

3. Strong VLF Fields and High Gain

Most whistler-mode interactions reach saturation in strong VLF fields as illustrated in Chapter IV. Figure 6-3 shows the result of a simulation reaching strong fields with a large

coupling, $\omega_h = 50\text{s}^{-1}$, at resonance, $v_o = 0$, and an initial field strength $b_o = 0.1\text{s}^{-1}$. This hot plasma frequency and initial wave field amplitude correspond to a hot electron density of $1/\text{m}^3$ and field strength of 1 pT. When using realistic hot plasma frequencies, saturation occurs quickly so the interaction time has been reduced to 0.1s. This interaction time is realistic with numbers reported by *Helliwell et al.* [Ref. 21]. In this figure, only the final position of 2000 sample electrons are shown. After the initial bunching time, $t_b \approx 0.004\text{s}$, the field growth is exponential, until saturation occurs at a field strength of $b_s \approx 2(\omega_h^4/4\omega)^{1/3} \approx 9.33\text{s}^{-1}$ [Ref. 25]. Saturation limits the final gain to about 41dB followed by five synchrotron oscillations of the trapped electrons at frequency [Ref. 25],

$$\omega_s = \sqrt{\omega |b_s|} \approx (\omega \omega_h^2)^{1/3} \approx 107\pi\text{s}^{-1} \quad (6.4)$$

In Figure 6-3, the electrons stay in closed phase-space orbits as indicated by the two lines draw on the phase-space graph. A few electrons fall outside these lines because the lines' position was determined by the last value of the VLF field and earlier values were slightly larger.

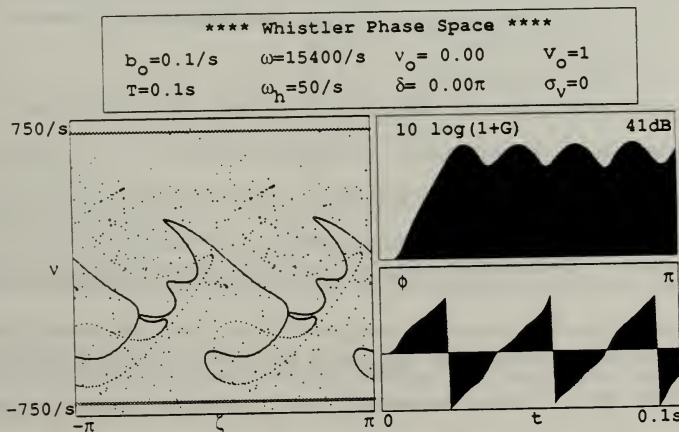


Figure 6-3. Electron phase-space, VLF wave power and phase for strong fields and high gain.

At this point, it is convenient to show that the dimensionless perpendicular velocity does not evolve significantly during the interaction time as was promised in the preceding chapter. Figure 6-4 shows the results of a simulation that was run using the same parameters as Figure 6-3. Instead of plotting the gain and VLF wave phase, the dimensionless perpendicular velocity, V , is plotted against the electron's perpendicular phase, θ . This figure shows the electrons stay very close to $V_o = 1$ while they bunch around two perpendicular phase points. The dimensionless perpendicular in a homogeneous magnetic field is driven by a term proportional to $2|b|$ which is small compared to the longitudinal phase velocity which is driven by a term proportional to $\omega V|b|$ with $V \approx 1$.

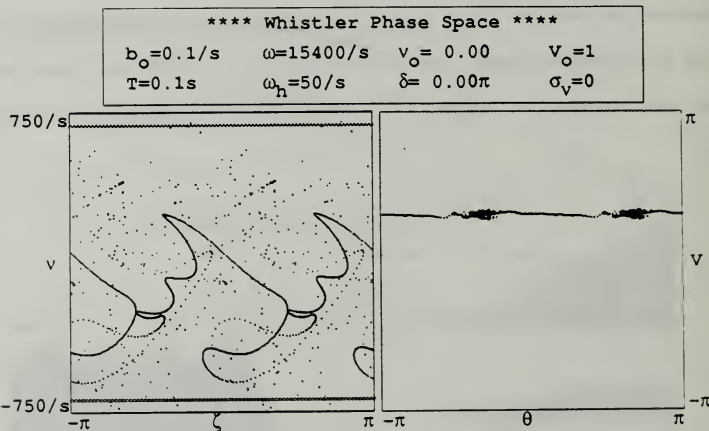


Figure 6-4. Electron phase-spaces (ζ, v) and (θ, V) for strong fields and high gain.

By solving the homogeneous equations of motion for a single VLF wave mode, we have been able to observe exponential growth, saturation, electron trapping, and synchrotron oscillations which are all nonlinear effects that occur in whistler-mode amplification and FELs. To make the simulations more realistic, the hot electrons are given a Gaussian spread in their initial phase velocity, $f(v) = \exp(-v^2 / 2\sigma_v^2) / \sqrt{2\pi}\sigma_v$,

with a standard deviation $\sigma_v = 200\text{s}^{-1}$ which corresponds to $\approx \pm 1\%$ of the resonant velocity. The simulation shown in Figure 6-5 has the same parameters as Figure 6-3 with the exception of the initial spread in phase velocities.

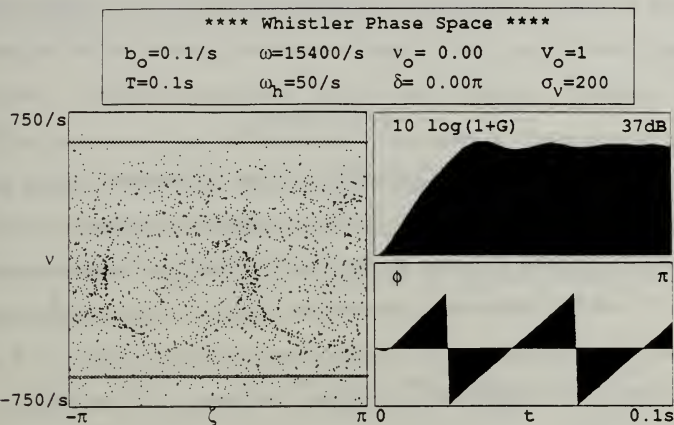


Figure 6-5. Electron phase-space, VLF wave power and phase for strong fields and high gain with a Gaussian spread in initial phase velocity.

In the phase-space plot, the Gaussian spread in phase velocity is centered around the resonant point, $v = 0$. The effects of the energy spread are immediately noticeable. The electrons continue to bunch around two electron phase points, but with much less distinction. The electrons are still in closed-path orbits as indicated by the gray lines. The gain drops significantly from 41dB to 37dB and the synchrotron oscillations are almost completely damped out. Also, the VLF wave phase advances more slowly than in Figure 6-3. These same effects are observed in a FEL when an initial energy spread is used.

B. SOLVING THE INHOMOGENEOUS EQUATIONS OF MOTION

1. Mono-Energetic Electron Beam in a Tapered Magnetic Field

To add even more realism to the simulations, the inhomogenous equations of motion are solved. Using the parameters from the experimental data, we can calculate the taper parameter

$$\delta = \frac{qc^2}{n^2} \approx 0.15\pi , \quad (5.60)$$

where $n \approx 30$, and $L \approx 5.1$. To study the effects of taper, it is necessary to again raise the interaction time to $T = 1s$. Figure 6-6 illustrates a simulation with taper, $\delta = 0.15\pi$. In this simulation, the initial VLF wave amplitude is $|b_o| = 0.01s^{-1}$, the hot plasma frequency is $\omega_h = 6s^{-1}$ and the dimensionless perpendicular velocity is $V_o = 1.0$. For the tapered simulations, the initial phase velocity is chosen so the electrons are resonant, $v = 0$, at time $t = T/2$, if there is no wave-particle interaction. The time $t = T/2$ corresponds to the geomagnetic equator.

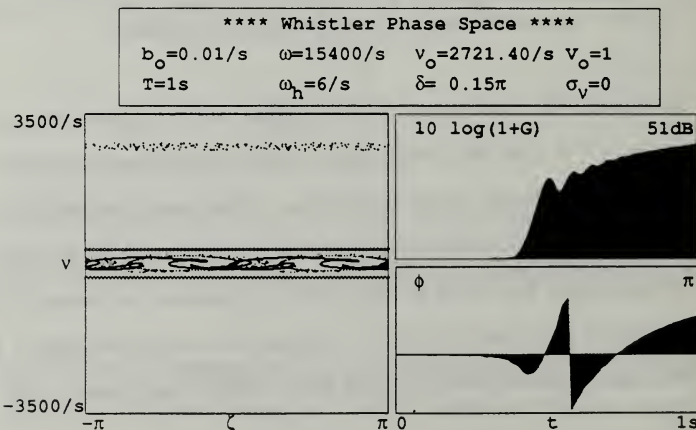


Figure 6-6. Electron phase-space, VLF wave power and phase for strong fields, high gain and a tapered magnetic field.

Since V_o is less than 2, the electrons start above resonance and move toward resonance with time. During this time, there is little interaction with the wave until the electrons are near resonance, $t \approx T/2$. At this point the VLF field grows exponentially with time as the phase initially decreases. While the electrons are near resonance, most of them become trapped and begin executing synchrotron oscillations. Also, the VLF wave's phase begins to increase. However, because the magnetic field is tapered, a significant number of electrons become untrapped and move away from resonance. These electrons are in open orbits and can be seen at the top of the phase-space plot in Figure 6-6. This causes the synchrotron oscillations to dampen out and delays the onset of saturation. To compare the effects of taper, Figure 6-7 is a simulation that uses the same parameters as Figure 6-6 except with no taper.

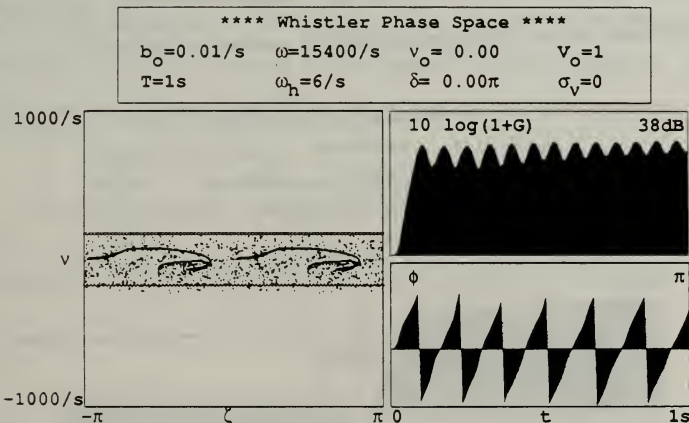


Figure 6-7. Electron phase-space, VLF wave power and phase for strong fields, high gain without tapering.

Since the electrons, in Figure 6-7, start out resonant, saturation occurs quickly since there is relatively good coupling, $\omega_h = 6s^{-1}$. The electrons stay trapped in closed phase-

space orbits and execute many synchrotron oscillations. Also, the VLF phase advances quickly in strong fields. However, because saturation occurs so quickly, the gain is limited to about 38dB. In the tapered case, Figure 6-6, saturation is delayed so the wave can continue to grow. At the end of the interaction time, the field's gain was still not saturated and had reached a level of 51dB. These same effects are observed in FELs. It should be noted that the scales on Figures 6-6 and 6-7 are different in order to show all of the effects.

In a tapered magnetic field, the dimensionless perpendicular velocity evolves differently than was seen in Figure 6-4 for a homogeneous magnetic field. Figure 6-8 illustrates this point by plotting the longitudinal and perpendicular phase-spaces for the same parameters that were used in Figure 6-6. For the electrons that are trapped in the strong potential well of the VLF wave, the V does not evolve much while the electrons bunch around two perpendicular phase points as was seen in Figure 6-4.

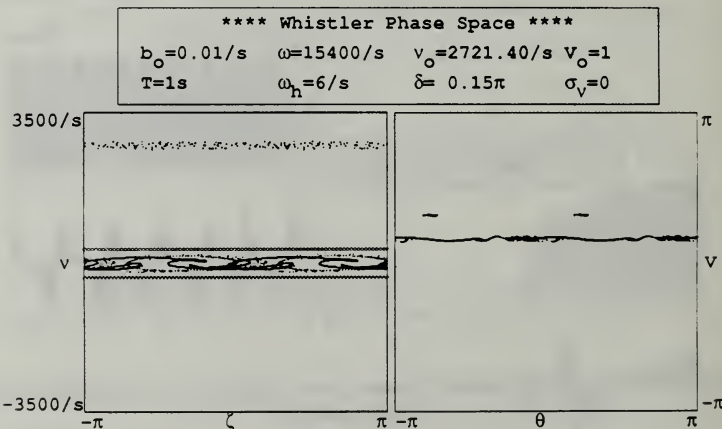


Figure 6-8. Electron phase-spaces (ζ, v) and (θ, V) for strong fields and high gain in a tapered magnetic field.

However, for the electrons that are not trapped and move away from resonance due to the tapered magnetic field, their dimensionless perpendicular velocity increases while bunching around two different perpendicular phase points.

2. Gaussian Distributed Electron Beam in a Tapered Magnetic Field

Next, the sensitivity to an initial energy spread is investigated. Figure 6-9 shows the results of a simulation run with the same parameters as Figure 6-7; except, the initial electron phase velocities were spread according to the Gaussian distribution used in the preceding section with $\sigma_v = 50s^{-1}$. This resulted in a gain decrease of about 5dB with dampen synchrotron oscillation amplitudes as was seen in the previous section. However, in Figure 6-10, the same spread and distribution is used on a system of electrons in a tapered magnetic field. Since the electrons start out so far off-resonance and move toward resonance, the spread, $\sigma_v = 50s^{-1}$, has less effect. Even though the final gain only drops by about 1dB, electron bunching is not as obvious as before in Figure 6-6. Again, the synchrotron oscillations are damped out more quickly due to the energy spread.

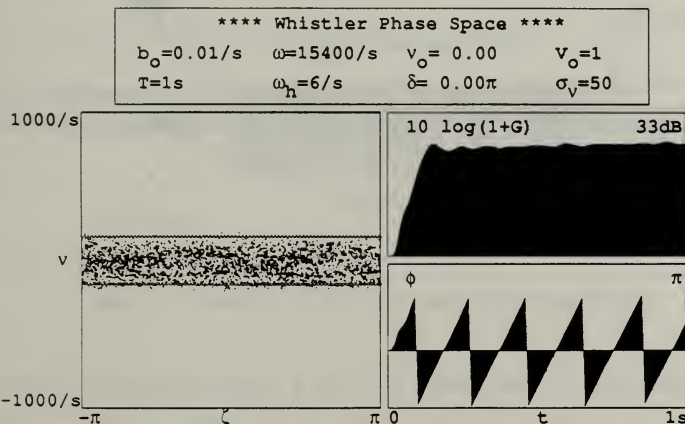


Figure 6-9. Electron phase-space, VLF wave power and phase for strong fields and high gain with a Gaussian spread in initial phase velocity.

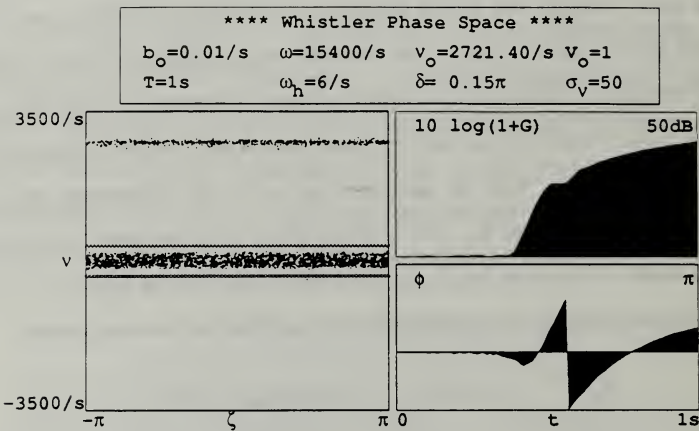


Figure 6-10. Electron phase-space, VLF wave power and phase for strong fields and high gain with a Gaussian spread in initial phase velocity and a tapered magnetic field.

VII. LIMIT-CYCLE BEHAVIOR IN THE CEBAF INFRARED FREE ELECTRON LASER (FEL)

A. FEL DESIGN AND OPERATION

Electron micropulses are the direct result of the typical accelerators used today. Most accelerators use RF microwave cavities to add energy to the electrons. Since only $\approx 3^\circ$ of the RF phase is used, the electron bunch that is accelerated must be small. Since the FEL operation depends on small electron pulses, the light produced will also be pulsed. When the optical wave envelope is comparable to the size of the electron micropulse, "short-pulse" effects can occur. This chapter will discuss a significant short-pulse effect known as limit-cycle behavior [Ref. 27].

A FEL consists of three major components: the electron accelerator, the undulator, and resonator as shown in Figure 7-1 [Ref. 7].

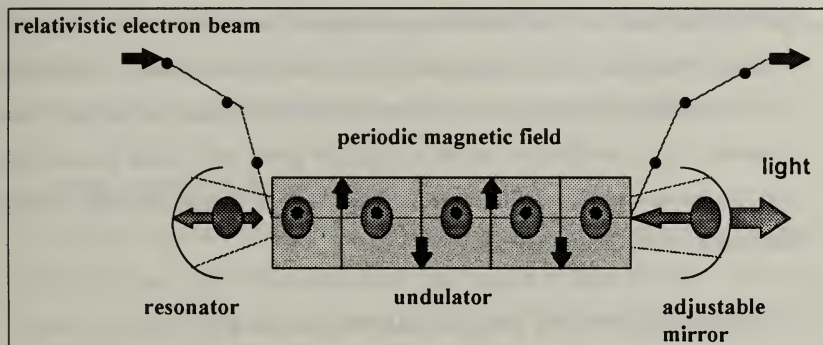


Figure 7-1. Schematic of a FEL showing the major components.

An electron accelerator produces a relativistic electron beam in small packets called micropulses. These micropulses are typically 1 mm of a side and contain approximately 10^{12} electrons. Micropulses are usually separated by several meters. Many micropulses in

sequence to form a macropulse. In many FEL designs, the accelerator can only produce a short length macropulse before the equipment must be cooled down. This is not the case at the Continuous Electron Beam Acceleration Facility (CEBAF) where supercooled components can continuously supply a "CW" macropulse.

After the electrons have been fully accelerated to speeds very close to the speed of light ($0.9999c$), they are passed through an undulator. The undulator consists of magnets that produce a transverse periodic magnetic field. The magnetic field strength in the electron vacuum tube is typically 1 T. The undulator causes the electrons to undergo periodic acceleration, which results in spontaneous radiation. The spontaneous radiation is stored in the resonator shown in Figure 7-1. The light pulse, produced by an electron micropulse, travels down to the end of the resonator and bounces back. The timing of the FEL has to be such that when the light pulse reenters the undulator, a new micropulse is entering also. After many passes, the light pulse and the electron micropulse couple together which leads to stimulated emission. New light is added to the existing light pulse to cause wave growth. This timing mechanism is called "synchronization". The coupling of the light to the micropulse causes the electrons to "bunch" in phase so that they radiate coherently. Once the light has reached a significant power level, it can be outcoupled from the resonator to be used for many purposes such as medical research, microchip lithography, or as a military weapon.

B. DESCRIPTION OF THE CEBAF IR FACILITY

The CEBAF began construction in 1987 in Newport News, Virginia to be used as a center for nuclear physics research. The CEBAF superconducting, recirculating accelerator will provide simultaneous electron beam energies from 0.8 to 4 GeV to three experimental halls. First operation of the accelerator for physics research is scheduled for 1994. [Ref. 28]

CEBAF's advanced accelerator physics and engineering capabilities will be used to construct and operate two free electron lasers (FELs) that would operate in the infrared, $\lambda = 3.6$ to $17 \mu\text{m}$, and in the ultra-violet, $\lambda = 150$ to 260 nm . Each FEL would produce average power outputs in the kilowatt range. [Ref. 28]

Two dimensional computer simulations following the evolution of short optical and electron pulses in coordinates t and z have predicted the CEBAF IR FEL will observe limit-cycle behavior. Limit-cycle power oscillations are caused by "marching subpulses" that grow at the trailing edge of the optical pulse through a super-radiant process, and pass through the main optical envelope. The power evolution exhibits steady-state oscillation as new optical pulses grow periodically [Ref. 29]. This behavior was predicted some time ago [Ref. 27]; however, only one experiment has observed this phenomenon [Ref. 30]. This effect is interesting because the FEL's output optical power oscillates even though all operation parameters are being held constant. The CEBAF IR FEL will provide an excellent platform for observing and investigating limit-cycle behavior because it produces a stable, continuous stream of high-quality electron micropulses comparable to the "slippage distance," $N\lambda$, where N is the number of periods in the undulator.

C. THE CEBAF IR FEL DESIGN

The first proposed CEBAF FEL, driven by the 45 MeV electron beam from the CEBAF Injector, will produce an average output power of approximately 1 kW at the baseline IR wavelengths of $\lambda \approx 3.6$ to $17 \mu\text{m}$ [Ref. 28]. The CEBAF IR FEL is summarized in Table 2.1. The CEBAF linacs will supply the FEL with a high-quality electron beam with a high average power of 800 kW and a low energy spread of $\Delta\gamma/\gamma = 0.001$. The electron beam kinetic energy of $(\gamma - 1)mc^2 = 45 \text{ MeV}$ yields a Lorentz factor of $\gamma = 89$, where m is the electron mass and c is the speed of light.

Table 7-1 CEBAF IR FEL SPECIFICATIONS. [Ref. 29]

Electron kinetic energy (E)	45 MeV
Pulse repetition frequency	7.485 MHz
Fractional momentum spread	2×10^{-3}
Electron bunch length	1 ps
Peak current (I_p)	60 A
Normalized emittance (ϵ_n)	15 mm-mrad
Undulator length (L)	1.5 m
Undulator Wavelength (λ_o)	6 cm
Number of periods (N)	25
Undulator type	electromagnetic
K (maximum)	2.1
K (nominal)	1.76
Maximum field (B)	0.54 T
Rayleigh length (Z_o)	0.75 m
Optical mode waist (W_o)	1.5 mm @ 10 μ m
Optical cavity length (S)	20.04 m
Electron beam radius (r_o)	0.031 cm

Pertinent dimensionless parameters describe the operation of the CEBAF IR FEL. The dimensionless electron beam current, j , determines the reaction of the optical field to the bunching of the electrons:

$$j = \frac{8N(e\pi KL)^2 \rho [JJ]^2}{\gamma^3 mc^2}, \quad (7.1)$$

where ρ is the electron beam particle density and $K = eB\lambda_o / 2\sqrt{2\pi}mc^2$ is the undulator parameter. The linearly-polarized undulator uses the factor " JJ ", where $JJ = J_o(\xi) - J_1(\xi)$; J_o and J_1 are Bessel functions, and $\xi = K^2 / 2(1 + K^2)$ [Ref. 23]. The FEL's wavelength is

$$\lambda = \left\{ \frac{1 + K^2}{2\gamma^2} \right\} \lambda_o, \quad (7.2)$$

and is tuned by adjusting the electron beam energy, γ , or K in the undulator. The dimensionless electron beam current can range between $j = 1$ to 5 for the CEBAF IR FEL depending on the K value and the length of the undulator. The shape of the electron beam

pulse is parabolic, where $j(z) = j(1 - 2z^2 / \sigma_z^2)$ for $j(z) > 0$, or otherwise zero, where the normalized electron pulse length is given by $\sigma_z = l_e/N\lambda \approx 1.4$ for the CEBAF IR FEL. The dimensionless beam current j is given by (7.1) and z is the electron micropulse position normalized to $N\lambda$.

While the optical pulse grows with each pass, optical losses in the resonator are determined by the Q value so that e^{-nQ} describes the decay in optical power over many passes n . Typical Q values range from 20 to 100 depending on resonator cavity design and optical outcoupling.

The desynchronization, $d = -\Delta S/N\lambda$, is a slight displacement of one of the resonator mirrors by ΔS . This displacement is used to alter the travel time of the rebounding light pulse in order to match the arrival of subsequent electron pulses [Ref. 29]. Exact synchronization between the light and the electron micropulse occurs when $d = 0$. Power output and limit-cycle behavior are sensitive to slight variations in d .

D. LIMIT-CYCLE BEHAVIOR

In strong optical fields, electrons can become trapped in deep potential wells created by the combined optical and undulator field forces. The optical field envelope displayed in Figure 7-3 has the dimensionless amplitude $a(z) = 4\pi NeKLE(z)/\gamma^2 mc^2$, where $E(z)$ is the complex optical electric field with all other terms previously defined. By looking at the phase-space evolution of the electrons, it is observed that a field strength of $|a| = 4\pi^2$ causes one oscillation of the trapped electrons. Electrons trapped near the bottom of the potential well oscillate at the synchrotron frequency given by $\nu_s = |a|^{1/2}$. The oscillation of the phase bunched electrons couples to the optical wave causing the amplitude, and the phase to oscillate at the synchrotron frequency leading to sideband formation and the trapped-particle instability. [Ref. 29]

For the CEBAF short-pulsed IR FEL, the optical pulse travels down the undulator at velocity c , while the electrons travel slightly slower with velocity $\beta_0 c$. The optical pulse

overtakes the electron pulse as they move down the undulator and are separated by the slippage distance, $N\lambda$ at the end of the undulator. As the electron pulse slips back relative to the optical pulse, the electrons continue to radiate coherently to form an optical subpulse. This process accounts for the predominant optical growth in the rear of the optical pulse. For typical FEL designs, the optical pulse is amplified preferentially in the rear of the pulse, because of the relative motion between the electrons and the optical pulse. As a result, the optical pulse centroid has a speed slightly less than c which must be accounted for by the desynchronization, d [Ref. 29]. Since d offsets the optical pulse relative to the new electron micropulse, the subpulse formed by the super-radiant process moves forward relative to the optical pulse. The subpulse's new spatial location is in a region of higher gain and begins to grow. After many more passes, the subpulse decreases in size as it moves to the front of the optical pulse into an electron deficient area of poor optical coupling and low gain. This process causes the optical amplitude to cycle in response to the train of subpulses that moves through it. This is illustrated in Figure 7-2 where the evolution of the optical amplitude is shown. The relative optical power and pass number are shown below each frame. The subpulses moving through the main optical envelope cause the shape of the envelope to change in a periodic fashion over approximately 120 passes. The net result of this process, over many passes, is to periodically change the shape under the optical spectrum and causes the optical power to oscillate as well. This oscillation in optical power, while holding all operational parameters constant, is known as "limit-cycle" behavior.

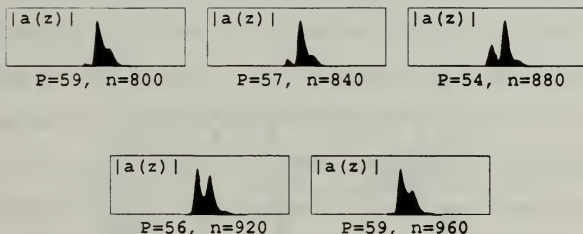


Figure 7-2. Snapshots of the optical pulse envelope as it evolves over 160 passes. The relative power and pass number are below each frame.

Figure 7-3 illustrates a simulation of the CEBAF IR FEL lasing at $\lambda = 10 \mu\text{m}$ with a desynchronization of $\Delta S = -2.5 \mu\text{m}$. From left to right, the three upper frames show the final optical pulse shape, optical spectrum, and electron energy spectrum at the end of the simulation. The middle three frames from left to right, show the evolution of the optical pulse shape, optical power spectrum, and electron energy spectrum versus the undulator pass number n . The bottom three frames display the electron pulse shape at the beginning and end of the slippage process, the gain spectrum, and the optical power versus the undulator pass number n . The slippage process is demonstrated by the relative positions of the parabolic electron pulses at the beginning, $\tau = 0$, and the end, $\tau = 1$, of the undulator where $\tau = ct/L$ is the dimensionless time. The spectral frames are plotted versus the dimensionless phase velocity $v = L[(k + k_o)\beta_z - k]$. The middle-left frame demonstrates how the optical amplitude grows and moves to the right of the main optical pulse over many passes. This results in periodic changes in the power spectrum width as seen in the middle-center frame. The oscillations in the power spectrum can be seen in the lower-left frame. The fractional amplitude of the total optical power is 11% and the period of oscillation is 135 for the typical CEBAF parameters shown in Table 7-1. The initial

optical amplitude $a_o = 1.0$ and initial phase velocity $v_o = 2.6$ do not affect the final results, but were selected so that the optical power would achieve steady-state in a fewer number of passes.

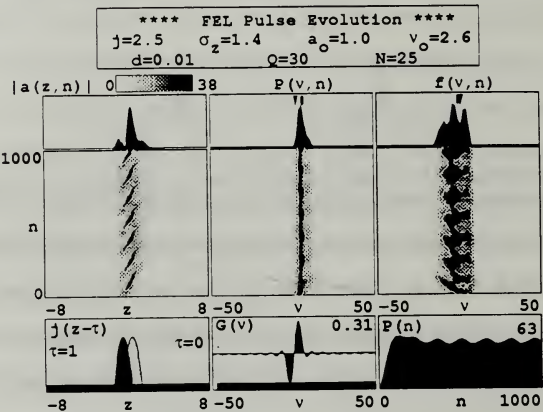


Figure 7-3. Simulation demonstrating the development of the optical amplitude, optical power and electron spectrums, and limit-cycle behavior.

To investigate limit-cycle behavior further, the dimensionless parameters j , σ_z , and Q are varied one at a time over the CEBAF IR FEL operating range. Simulations were run and the fractional amplitude and frequency of oscillation were measured from figures similar to Figure 7-3. The fractional amplitude is the average peak-to-trough height divided by the average power once in steady-state. The relative frequency is the inverse of the limit-cycle period normalized to the average period. The results of varying the electron pulse length between 0.015 to 0.055 cm while $j = 2.5$, $Q = 30$, and $d = 0.01$ are displayed in Figure 7-4. When σ_z is small, a lower limit threshold effect is observed until

$\sigma_z = 0.8$, then limit-cycle behavior begins. While σ_z is small, poor coupling between the electron and optical pulses lead to lower optical field strengths. The optical field strength is too low to cause the trapped-particle instability and side-band formation, so little or no limit-cycle behavior is observed. This is illustrated in Figure 7-5. When σ_z is too large, optical fields are large enough to cause the trapped-particle instability and subpulses. These subpulses grow and move through the main optical pulse as seen in Figure 7-6. However, the area under the optical amplitude curve does not change significantly with time. Therefore, once steady-state is reached, the optical power does not vary in time and limit-cycle behavior diminishes.

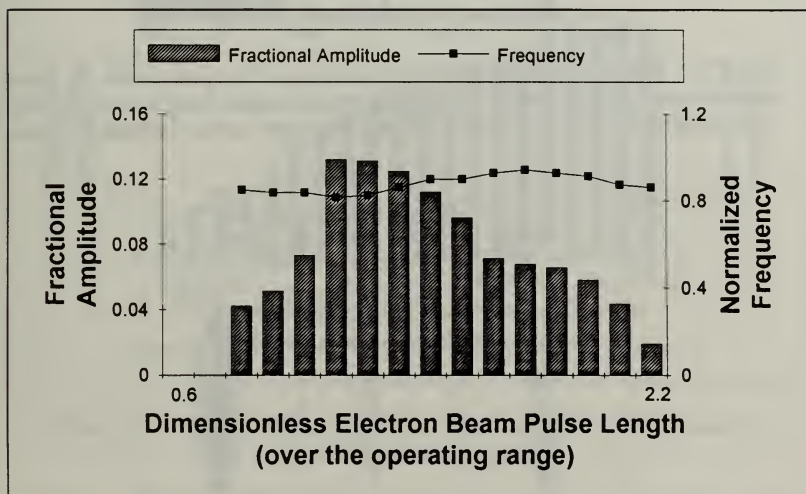


Figure 7-4. Plot of the limit-cycle fractional amplitude and frequency versus the electron micropulse length.

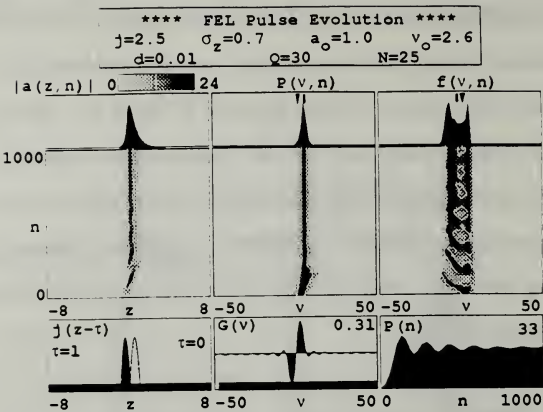


Figure 7-5. Simulation demonstrating the development of the optical amplitude, optical power and electron spectrums for a short electron pulse length. Note poor overlap of the electron pulse and optical pulse lead to weak optical fields and no sideband formation.

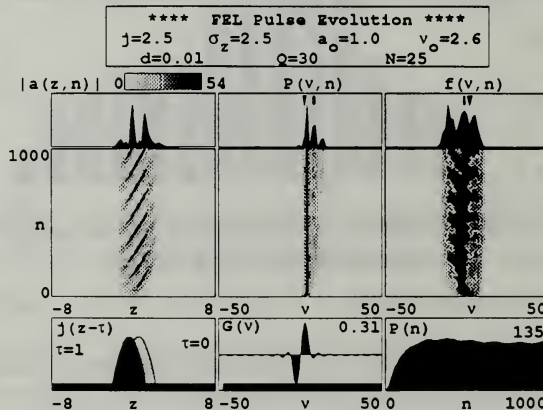


Figure 7-6. Simulation demonstrating the development of the optical amplitude, optical power and electron spectrums for a large electron pulse length. Note good overlap of the electron pulse and optical pulse lead to strong fields, trapped-particle instability, and sidebands, but no limit-cycle behavior.

Figure 7-7 shows the limit-cycle response as the dimensionless electron beam current is varied over the operating range while $\sigma_z = 1.4$, $Q = 30$, and $d = 0.01$. The fractional amplitude follows changes in j and the frequency changes very little over the operating range. Once j is increased to ≥ 3.5 , the sidebands are unstable and the optical power becomes chaotic. It would appear, at first, that only increasing the amount of charge in the electron micropulse causes the fractional amplitude to change.

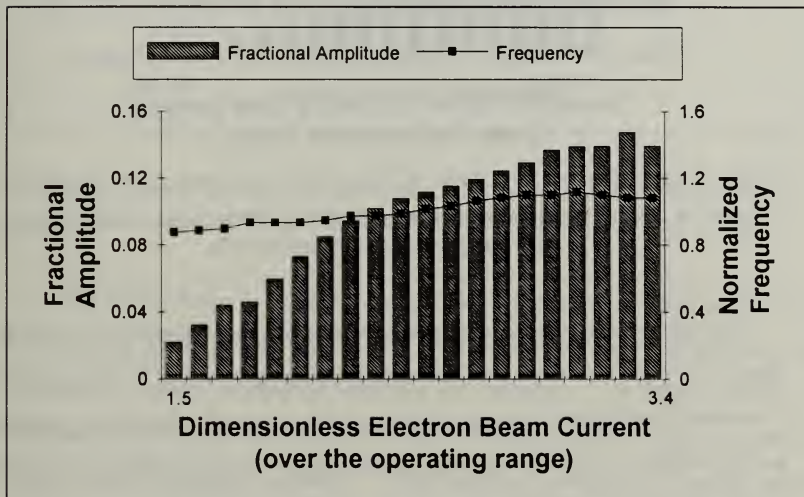


Figure 7-7. Plot of the limit-cycle fractional amplitude and frequency versus the dimensionless electron current.

Therefore, this was investigated by holding the total charge in the electron micropulse constant. When j is increased, σ_z is decreased to keep their product constant. The results of these simulations are shown in Figure 7-8. The fractional amplitude of the limit-cycle power oscillations follows j , and does not remain constant with constant total charge. The fractional amplitude is greatest when j is large and σ_z is small.

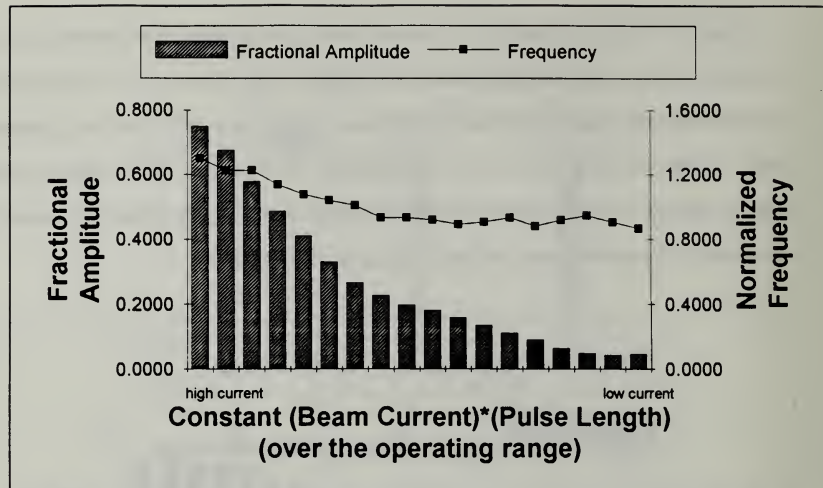


Figure 7-8. Plot of the limit-cycle fractional amplitude and frequency while holding the total charge in the micropulse constant.

The limit-cycle response to variations in the resonator loss parameter, Q , is shown in Figure 7-9. These simulations were made while maintaining $j = 2.5$, $\sigma_z = 1.4$ and $d = 0.01$. As expected, the fractional amplitude increases as Q is increased so that optical amplitudes are large enough to cause the trapped-particle instability. Steady-state limit-cycle behavior begins when $Q \geq 30$ while the frequency is constant throughout the entire range. Chaotic behavior was observed when $Q \geq 50$, and determines the upper limit of Figure 7-9.

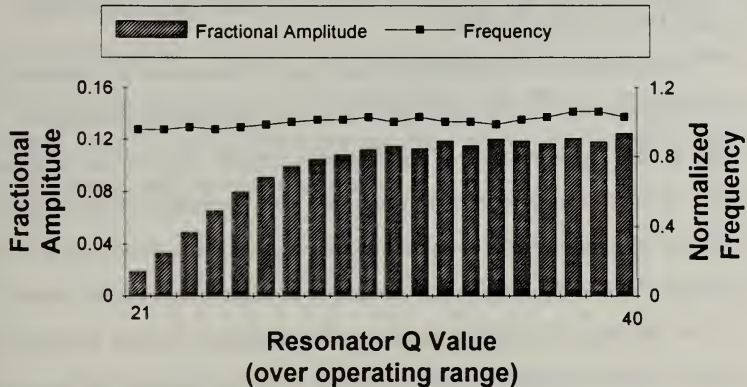


Figure 7-9. Plot of the limit-cycle fractional amplitude and frequency while holding the total charge in the micropulse constant.

Limit-cycle behavior is interesting because the optical power oscillates even though all operational parameters are held constant. Few facilities are capable of observing this phenomenon, because engineering constraints and limitations. The CEBAF IR FEL is predicted to observe limit-cycle behavior because of the high-quality, continuous stream of stable electron micropulses employed. Using computer simulations, the optical power oscillations due to limit-cycle behavior are observed over the entire operating range of the CEBAF IR FEL. The effects are most pronounced for large j , moderate d , and $Q \leq 50$. For the parameters used in this thesis, limit-cycle oscillation amplitudes follow the optical field amplitude unless j is a competing parameter, in which case the oscillation amplitudes follow j .

E. SIMILARITIES BETWEEN FELS AND WHISTLER-MODE AMPLIFICATION (WMA)

The experimental development of whistlers and the theoretical development of FELs has steadily matured over the years, each with its own successes and shortcomings. In this thesis, a study has been made of the interaction between electrons and whistler-mode waves from the FEL viewpoint. Because of the many similarities between whistlers and FELs, a fresh insight into the complex world of magnetospheric phenomena could lead to benefits for both communities. Some of the areas common to both subjects include:

1. The FEL and the whistler interaction utilize electrons in periodic transverse motion coupled to electromagnetic radiation. In both cases, the electrons are accelerated by magnetic fields that cause their "macroscopic" motion.
2. Amplification in both the FEL and the whistler involves narrow band radiation that can be amplified by several thousand.
3. The evolution of the "microscopic" motion of the electrons in phase-space is described by the pendulum equation for both the FEL and the whistler.
4. A microwave FEL utilizes a waveguide with a dispersion relationship, $n\omega = ck$, just as the ducted VLF wave does.
5. The electron distribution functions are important to both the FEL and whistler-mode amplification.
6. Tapered magnetic fields occur naturally in the magnetosphere, and are also used in FELs to increase the amplification after saturation.
7. Non-linear effects such as saturation, particle-trapping, and synchrotron oscillations are common to both systems.
8. Simple mathematical relationships that predict weak/strong field regimes, low/high gain regimes, bunching times, the trapped-particle synchrotron frequency, and the final gain levels are common to both systems. [Ref. 26]

There are numerous benefits to modeling the whistler interaction region using established FEL physics. Being able to use a ground-based FEL to study the interactions that occur in the magnetosphere allows reproducible, cost effective experiments to be conducted. On the other hand, better understanding of whistler-mode amplification would enhance communication and navigation systems.

VIII. SUGGESTIONS FOR FUTURE WORK

A. FURTHER ANALYSIS OF SIPLE STATION DATA

The analysis of the data received from Siple Station has only begun. In this thesis, macroscopic characteristics of the data were investigated. Simple correlations between saturated power levels were made. Further analysis is required to answer many scientific questions about the data:

- (1) What is the role and importance of triggered emissions in explaining the observed wave phenomena?
- (2) How does the triggered emission growth and frequency dependence change over different time scales?
- (3) Which cold and hot plasma parameters could, in principle, be derived from measurements made of the VLF wave's growth and saturation?
- (4) Which time variations are attributed to propagation effects such as ionospheric transmission or loss, and which variations are attributed to hot plasma effects?
- (5) What is the range of energies and pitch angles for the hot electrons in order to explain the observed experimental data?
- (6) What is the potential for hot plasma diagnostics using both ground based wave injection facilities and natural whistler signals?
- (7) Are the time variations seen in the 10 hour segment analyzed consistent with the data after that period?

B. IMPROVEMENTS TO THE SIMULATION

The simulation used up to this point properly handles the inhomogeneous geomagnetic field and allows for initial energies to be spread randomly using a Gaussian distribution. This distribution, however, is too simplistic. Data analyzed by *Schield* and *Frank* [Ref. 31] indicate that the electrons may be distributed according to an inverse

power law, E^{-n} with n ranging from 2 to 4 for electrons with energies between 1 and 6 keV. However, the complications do not stop there. Not only must the electron's total energy be distributed properly, but their pitch angles must also be distributed correctly with the loss cone in mind. The problem with the distribution functions $f(v)$ and $g(V)$ is complicated because they may vary significantly with magnetic activity and particle injection events. Also, the lack of satellite data for electrons with energies ≈ 1 keV at large L values greater than four makes formulating a distribution function that much more difficult.

Up to now, little progress has been made to accurately describe triggered emissions. Some simulations show emissions sweeping over small a frequency range, but none have predicted sweeps that match the observed changes of 500 Hz out of 2500 Hz. [Refs. 32 and 33]. Therefore, further theoretical work needs to be done in order to predict the endless amount of observed triggered emission data.

Even though sidebands were produced in the simulations due to the trapped-particle instability, the origin of the observed experimental sidebands is still under question. Some ideas are that the sidebands are the result of VLF signal modulation with the Canadian power grid, or signal modulation with the transmitter auxiliary equipment [Ref. 33]. Another idea is that the VLF waves are transmitted into different lateral ducts. This would cause a small phase shift between the waves due to their different paths which would cause a low frequency modulation, but no change in the reception time-delay of the signals would be noticed. In either case, this issue needs to be resolved.

C. MORE ON LIMIT-CYCLE BEHAVIOR

Many simulations were run using the nominal CEBAF IR FEL parameters in order to investigate the severity of limit-cycle behavior. However, explanations that describe the results of the variations seen in the dimensionless current, resonator Q , and constant total charge have not been made. The results presented in Chapter VII need to be investigated

more closely in order to offer a theoretical explanation. Also, simulations need to be performed that vary the desynchronism while monitoring the limit-cycle fractional amplitude. Therefore, the results could be compared to the experimental results recently seen in Holland [Ref. 30].

IX. CONCLUSIONS

Whistler waves and triggered emissions have long been a source of signal degradation for military communication and navigation systems. The Navy's primary interest in whistlers arose because of the strong need for clear, uninterrupted VLF communications with ballistic submarines. Motivation for the study of whistlers is outlined in Chapter II. Siple Station was an excellent platform for launching VLF waves to (1) study the effects of VLF wave propagation through the magnetosphere, (2) better understand the magnetospheric wave-particle interaction, including wave-growth, saturation, sidebands, and triggered emissions, (3) form the methodology for a hot plasma diagnostic tool, and (4) describe the time scales over which magnetospheric events take place.

In order to compare the saturation level of one amplified signal to another, the propagation conditions must be known, or at least constant. In the data presented in Chapter IV, the propagation conditions were assumed to be constant. This assumption is valid because (1) the time-delay between the transmitted and received signals was constant over the period, (2) the signal strengths for Signals #2a and #2b were constant over the period, (3) no evidence of multipath propagation for the frequency ramps was observed, and (4) no temporal spreading of constant frequency pulses was observed. Therefore, the difference between the relative saturation levels of two signals can be attributed to hot plasma effects. By normalizing all of the relative power levels to the same initial power level, as was done in Chapter IV, relative gain in the interaction region was obtained. Using computer simulations, as in Chapter VI, to "fit" most of the observed variations of the data, an idea of the hot electron density responsible for those variations was obtained.

By observing the variations seen in the saturation levels of the transmitted data, trends are established that determine a characteristic time scale that gives insight into what type of phenomena caused the variation. By comparing two similar signals, saturation levels remained constant over about a 30 second time scale. Yet, signals could change abruptly

over a 5-15 minute and 1-2 hour time scale. Assuming an interaction length of ≈ 2000 km [Ref. 34], a typical interaction time would be 0.1 second. Also, from Chapter III, a nominal bounce time is 6 seconds. Both the interaction time and the bounce time occur too quickly to explain the variations seen in the data. However, the drift motion of an electron out of a field-aligned duct can take ≈ 30 minutes, and injection events of new hot electrons can occur over 5 minutes to many hours. Both of these events could be used to explain the variations seen in the experimental data.

The wave-particle interaction between a hot electron and a VLF wave is non-linear. Therefore, effects can occur that would not be possible in a linear amplification system. A notable non-linear effect that was observed for these data was a threshold power. The threshold power is a power level a signal must be above before exponential wave-growth occurs. Experimental evidence that confirms the presence of a threshold power include (1) signal strengths for the left-hand polarized waves were below the threshold power, and therefore did not amplify, (2) direct measurements of the threshold power were possible using the transmitted power ramp, Signal #7, and (3) initial transmitted power levels for Signal #5 were above the threshold power, and therefore demonstrated exponential growth immediately.

Computer simulations are used in Chapter VI that solve the self-consistent equations of motion for each hot electron in the presence of a VLF wave and the earth's magnetic field. These simulations show that the electrons bunch around two points in one wavelength of light. The amount of gain is primarily dependent on the density of hot electrons and to a lesser extent on, the input wave amplitude (b_o), the initial perpendicular velocity (V_o), and the initial phase velocity (v_o). This occurs for both the homogeneous and non-homogeneous cases. Also, the presence of the tapered magnetic field causes four distinguishing characteristics to be noted. First, the onset of wave-growth is delayed until the electrons move closer into resonance. Second, there is a phase decrease until saturation occurs, then the wave's phase advances. For the homogeneous case, the VLF

wave's phase advances immediately. Third, for the tapered case, the steady-state synchrotron oscillations damp out as the electrons move out of the region of the strong VLF field. For the homogeneous case, the electrons remained trapped in the VLF wave's potential well and execute synchrotron motion. Fourth, using an energy spread had less of an effect on the tapered simulations than the non-tapered simulations. In fact, using an energy spread had little or no effect on the final power obtained in the tapered simulations, but did affect the phase and synchrotron motion.

Finally, limit-cycle behavior in the CEBAF IR FEL is discussed in Chapter VII. The severity of the limit-cycle behavior is measured in terms of the fractional amplitude of the oscillations. These oscillations were observed across the operating range for the CEBAF IR FEL parameters. In particular, the electron pulse length, dimensionless current, constant total charge, and resonator Q were varied while monitoring the fractional amplitude and frequency of limit-cycle oscillations. These results are plotted in Chapter VII. Limit-cycle oscillations were most severe for large electron beam current, low resonator losses, and moderate values of the electron pulse length.

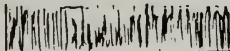
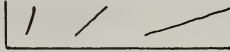
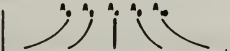
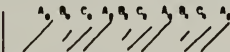
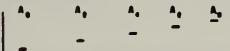
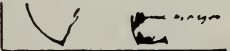
Suggestions for further work are presented in Chapter VIII. These include a more detailed look at the Siple Station data in order to correlate the growth rates to the saturation levels. There is a need to find more clear-cut cases where the threshold power level effect can be seen. Computer simulations for the VLF wave-particle interactions need to include realistic energy distributions. More theoretical work needs to be accomplished in order to explain triggered emissions. Limit-cycle behavior needs to be studied while varying the desynchronism in order to compare the results that were seen recently in Holland [Ref. 30]. A strong, continuing effort needs to be put forth in order extract the advantages from both the whistler interaction and FELs.

APPENDIX A. ATLAS OF WHISTLER AND TRIGGERED EMISSION TYPES [REF. 2]

WHISTLER TYPES

Type and Definition	Spectral Form
I. One-hop (short) A whistler that has traversed one complete path through the ionosphere.	
II. Two-hop (long) A whistler that has traversed in sequence two complete paths through the ionosphere. The two paths may or may not be the same.	
III. Hybrid A combination of a one-hop and a two-hop whistler originating in the same source.	
IV. Echo train	
A. Odd order: A succession of echoes of a one-hop whistler. Delays usually in ratio 1:3:5:7, etc. Components called one-hop, three-hop, five-hop, etc.	
B. Even order: A succession of echoes of a two-hop whistler. Delays usually in ratio 2:4:6:8, etc. Components called two-hop, four-hop, six-hop, etc.	
V. Multiple-component	
A. Multipath: A whistler with two or more components, each of which has traversed a different path through the ionosphere.	
B. Mixed-path: A multiple whistler of two or more hops in which combinations of the basic one-hop paths occur.	
VI. Multiple-source (multi-flash)	
Two or more whistlers closely associated in time, but having different sources.	
VII. Nose	
A whistler whose frequency-time curve exhibits both rising and falling branches. The delay is a minimum at the nose frequency f_n .	
VIII. Fractional-hop	
A whistler that has completed only a fraction of a one-hop path (often observed from a probe or satellite).	

MOORE SPECTRAL FORMS OF VLF EMISSIONS

Type and Name	Model Spectral Form
I. <i>His</i>	
II. <i>Discrete emissions</i>	
A. <i>Rising tone</i>	
B. <i>Falling tone</i>	
C. <i>Hook</i>	
D. <i>Combinations</i>	
III. <i>Periodic emissions</i>	
A. <i>Dispersive</i>	
B. <i>Non-dispersive</i>	
C. <i>Multiphase</i>	
D. <i>Drifting</i>	
IV. <i>Chorus</i>	
V. <i>Quasi-periodic emissions</i>	
VI. <i>Triggered emission</i>	

APPENDIX B. SAMPLE CALCULATION OF EXPERIMENTAL PARAMETERS IN THE INTERACTION REGION USING MATHCAD 3.1®

Input required constants and initial conditions:

Earth's radius:

$$R_0 = 6370000 \cdot \text{m}$$

L-shell:

$$L = 5.1$$

Equatorial pitch angle:

$$\alpha_0 = \frac{30 \cdot \pi}{180} \cdot \text{rad}$$

Electron charge:

$$e = 1.6 \cdot 10^{-19} \cdot \text{coul}$$

Electron mass:

$$M = 9.315 \cdot 10^{-31} \cdot \text{kg}$$

Electron energy:

$$E = 1500 \cdot (1.6 \cdot 10^{-19}) \cdot \text{joule}$$

Compute the radial distance of the magnetic field line as a function of latitude:

Geomagnetic latitude
of field line at R_0 :

$$\lambda_0 = \arccos\left(\frac{1}{\sqrt{L}}\right)$$

Geocentric radius:

$$R(\lambda) := R_0 \cdot \left(\frac{\cos(\lambda)}{\cos(\lambda_0)}\right)^2$$

For this example:

$$\lambda_0 = 63.717 \cdot \text{deg}$$

Compute the gyro-frequency (Hz) of the electron as a function of latitude [Ref. 2]:

$$f(\lambda) = 886000 \cdot \left(\frac{R_0}{R(\lambda)}\right)^3 \cdot \sqrt{1 + 3 \cdot \sin(\lambda)^2}$$

Compute the adiabatic invariant (μ) at the equator [Ref. 19]:

$$\mu = \frac{\left(\frac{e}{M}\right) \cdot E \cdot (\sin(\alpha_0))^2}{2 \cdot \pi \cdot f(0)}$$

Compute the arc length (m) from the equator as a function of latitude [Ref. 2]:

$$s(\lambda) = \frac{1}{2} \cdot \frac{R_0}{\left[(\cos(\lambda_0))^2 \cdot \sqrt{3} \right]} \cdot \left[\operatorname{asinh}(\sqrt{3} \cdot \sin(\lambda)) + (\sqrt{3} \cdot \sin(\lambda) \cdot \cosh(\operatorname{asinh}(\sqrt{3} \cdot \sin(\lambda)))) \right]$$

Compute the parallel velocity (m/sec) of the electron as a function of latitude:

$$v_{pl}(\lambda) = \sqrt{\left(2 \cdot \frac{E}{M} \right) - \left(4 \cdot \pi \cdot \mu \cdot \frac{f(\lambda)}{e} \right)} \quad \text{Compute bounce latitude: } \lambda_b = 0.57$$

Compute the perpendicular velocity (m/sec) and the pitch angle:

$$v_{pd}(\lambda) = \sqrt{\left(2 \cdot \frac{E}{M} \right) - v_{pl}(\lambda)^2} \quad \alpha(\lambda) = \arccos \left(\frac{v_{pl}(\lambda)}{\sqrt{2 \cdot \frac{E}{M}}} \right)$$

Compute the differential arc length element:

$$ds(\lambda) = \frac{d}{d\lambda} s(\lambda)$$

Compute the bounce period (sec):

$$\tau_b(\lambda) = 4 \cdot \int_0^{\lambda} \frac{ds(\lambda)}{v_{pl}(\lambda)} d\lambda \quad \tau_b(\lambda_b) = 5.151 \text{ sec}$$

Check the bounce period using different formulation [Ref. 11]:

Compute the total velocity (m/sec):

$$v = \sqrt{\left(2 \cdot \frac{E}{M} \right)} \quad v = 2.27 \cdot 10^7 \cdot \frac{\text{m}}{\text{sec}}$$

Form the Liemohn (1961), Hess (1968) and Roederer (1970) function [Ref. 35]:

$$F(\lambda) = \cos(\lambda) \cdot \frac{\sqrt{1 + 3 \cdot \sin(\lambda)^2}}{\sqrt{1 - \left[\frac{\sin(\alpha\lambda)^2 \cdot \sqrt{(1 + 3 \cdot \sin(\lambda)^2)}}{\cos(\lambda)^6} \right]}}$$

Form the bounce period integral equation:

$$\tau_b(\lambda b) = 4 \cdot R \cdot \frac{L}{v} \int_0^{\lambda b} F(\lambda) d\lambda$$

Calculate the bounce period (sec): (Same result as above)

$$\tau_b(\lambda b) = 5.151 \cdot \text{sec}$$

Input additional parameters:

Equatorial electron density (e/cc):	VLF wave frequency (Hz):	Speed of light:	Angular velocity constant for electrons [Ref. 35]
-------------------------------------	--------------------------	-----------------	---

$$N_{eo} = \frac{1.1 \cdot 10^4}{L^3} \quad f_w = 2450 \quad c = 3.0 \cdot 10^8 \cdot \frac{\text{m}}{\text{sec}} \quad a = 6.1087 \cdot 10^{-4} \cdot \frac{\text{rad}}{\text{sec}}$$

Compute the angular bounce drift velocity function [Ref. 35]:

$$V(\lambda) = a \cdot R \cdot L^2 \cdot \frac{v^2}{c^2} \cdot \left[3 - \left[2 \cdot \sin(\alpha\lambda)^2 \cdot \frac{\sqrt{(4 - 3 \cdot \cos(\lambda)^2)}}{\cos(\lambda)^6} \right] \right] \cdot \left[\frac{(1 + \sin(\lambda)^2) \cdot \cos(\lambda)^5}{\sqrt{(4 - 3 \cdot \cos(\lambda)^2)}} \right]$$

Compute the average drift period (hr) [Ref. 35]:

$$\phi_{avg} = \left(\frac{4}{\tau_b(\lambda b) \cdot v} \right) \cdot \left[\int_0^{\lambda b} \frac{V(\lambda) \cdot \sqrt{(4 - 3 \cdot \cos(\lambda)^2)}}{\cos(\lambda)^2 \cdot \cos(\alpha(\lambda))} d\lambda \right] \quad \tau_d = 2 \cdot \frac{\pi}{\phi_{avg}} \quad \tau_d = 56.776 \cdot \text{hr}$$

Form a range of latitudes:

$$i = 0 \dots 10 \quad \lambda r_i = \frac{\lambda b \cdot i}{10} \text{ rad}$$

Convert the gyro and VLF wave frequency to angular units:

$$\Omega(\lambda) = 2 \cdot \pi \cdot f(\lambda) \cdot \frac{\text{rad}}{\text{sec}} \quad \omega = 2 \cdot \pi \cdot f_w \cdot \frac{\text{rad}}{\text{sec}}$$

Compute the dipole approximation function and the electron density profile [Ref. 20]:

$$D(\lambda) = \left[1 + 4.5 \cdot \left(\frac{s(\lambda)}{L \cdot Ro} \right)^2 \right] \quad Ne(\lambda) = Ne_0 \cdot D(\lambda)$$

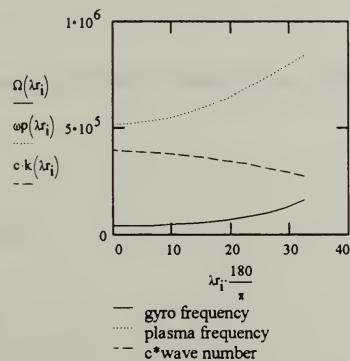
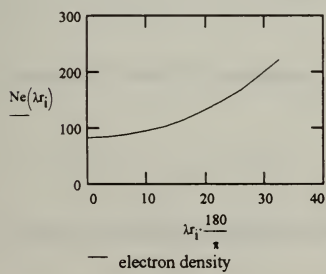
Compute the plasma frequency:

$$\omega_p(\lambda) = 18000 \cdot \pi \cdot \sqrt{Ne(\lambda)} \cdot \frac{\text{rad}}{\text{sec}}$$

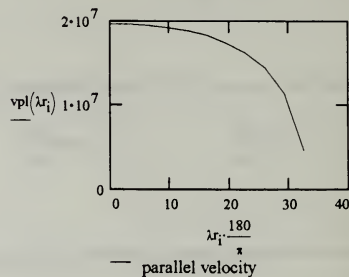
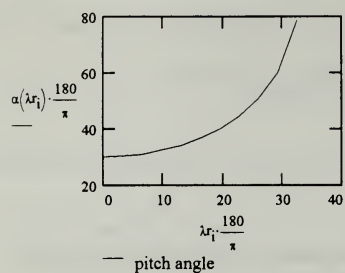
Compute the wave number:

$$k(\lambda) = \frac{1}{c} \cdot \omega \cdot \sqrt{1 + \frac{\omega_p(\lambda)^2}{\omega (\Omega(\lambda) - \omega)}}$$

Plot the electron density (e/cc), gyro-frequency, and the plasma frequency versus latitude from the equator:



Plot the pitch angle and parallel velocity component (m/sec) versus latitude from the equator:



APPENDIX C. PERFORMANCE CALCULATION OF THE SIMPLE STATION HORIZONTAL DIPOLE ANTENNA USING MATHCAD 3.1®

Enter the input parameters in MKS:

Antenna frequency, phase velocity, intrinsic impedance, length and height above ground [Ref. 12]:

$$f = 7750 \cdot \text{sec}^{-1} \quad v_p = 2.17 \cdot 10^8 \cdot \frac{\text{m}}{\text{sec}} \quad \eta_1 = 415 \cdot \text{ohm} \quad L = 42000 \cdot \text{m} \quad h = 6.0 \cdot \text{m}$$

Enter the free space intrinsic impedance and permeability:

$$\eta_0 = 377 \cdot \text{ohm} \quad \mu = 4 \cdot \pi \cdot 10^{-7} \cdot \frac{\text{henry}}{\text{m}} \quad i = \sqrt{-1}$$

Compute the wavelength, wave number and angular frequency:

$$\lambda = \frac{v_p}{f} \quad k = 2 \cdot \frac{\pi}{\lambda} \quad \omega = 2 \cdot \pi \cdot f$$

Enter the attenuation coefficient (α) and phase shift constant (β) for free space (0) and the antenna (1):

$$\alpha_0 = 0 \quad \beta_0 = 0 \quad \alpha_1 = 1.7 \cdot 10^{-5} \quad \beta_1 = 2.2 \cdot 10^{-4}$$

Compute the complex propagation constant for free space (0) and antenna (1) [Ref. 12]:

$$\gamma_0 = \alpha_0 + i \cdot \beta_0 \quad \gamma_1 = \alpha_1 + i \cdot \beta_1$$

Compute the reflection coefficient [Ref. 15]:

$$R_h(\theta) = \frac{\eta_1 \cdot \cos(\theta) - \eta_0 \cdot \cos\left(\arcsin\left(\frac{\gamma_0}{\gamma_1} \cdot \sin(\theta)\right)\right)}{\eta_1 \cdot \cos(\theta) + \eta_0 \cdot \cos\left(\arcsin\left(\frac{\gamma_0}{\gamma_1} \cdot \sin(\theta)\right)\right)}$$

Enter the antenna's current distribution and the rectangular-to-polar conversion function [Refs. 12 & 15]:

$$I(x) = \left(\frac{3}{2} \cdot \cos \left(\frac{2 \cdot \pi \cdot x}{14640 \cdot m} \right) + \frac{5}{2} \right) \cdot \text{amp} \quad \delta(\theta, \phi) = \sin(\theta) \cdot \cos(\phi)$$

Formulate an intermediate integral over the antenna's length and the spherical coordinate radial function to be used in next step [Ref. 15]:

$$\text{INT}(\theta, \phi) = \int_{-\frac{L}{2}}^{\frac{L}{2}} I(x) \cdot \exp(i \cdot k \cdot x \cdot \delta(\theta, \phi)) dx \quad g(r) = \frac{\mu \cdot \exp(-i \cdot k \cdot r)}{4 \cdot \pi \cdot r}$$

Compute the vector potential in spherical coordinates [Ref. 15]:

$$A1(r, \theta, \phi) = \begin{bmatrix} \cos(\phi) \cdot g(r) \cdot \text{INT}(\theta, \phi) \\ 0 \cdot \text{kg} \cdot \text{m} \\ \frac{0 \cdot \text{kg} \cdot \text{m}}{\text{coul} \cdot \text{sec}} \\ -\sin(\phi) \cdot g(r) \cdot \text{INT}(\theta, \phi) \end{bmatrix}$$

$$A(r, \theta, \phi) = A1(r, \theta, \phi) \cdot (\exp(i \cdot k \cdot h \cdot \cos(\theta)) + R_h(\theta) \cdot \exp(i \cdot k \cdot h \cdot \cos(\theta)))$$

Compute the electric and magnetic field vectors from the vector potential [Ref. 15]:

$$E(r, \theta, \phi) = -i \cdot \omega \cdot \begin{bmatrix} \frac{0 \cdot \text{kg} \cdot \text{m}}{\text{coul} \cdot \text{sec}} \\ A(r, \theta, \phi)_1 \\ A(r, \theta, \phi)_2 \end{bmatrix} \quad H(r, \theta, \phi) = \frac{\omega}{\eta l} \cdot \begin{bmatrix} \frac{0 \cdot \text{kg} \cdot \text{m}}{\text{coul} \cdot \text{sec}} \\ -A(r, \theta, \phi)_2 \\ A(r, \theta, \phi)_1 \end{bmatrix}$$

Compute the Poynting vector magnitude (S) and prepare it for integration (F) [Ref. 15]:

$$S(r, \theta, \phi) = \frac{1}{2 \cdot \eta_1} \cdot E(r, \theta, \phi) \cdot \overline{E(r, \theta, \phi)} \quad F(r, \theta, \phi) = S(r, \theta, \phi) \cdot r^2 \cdot \sin(\theta)$$

Integrate the Poynting vector in spherical coordinates over the upper hemisphere of the antenna to obtain the total power radiated in Watts [Ref. 15]:

$$\text{Power}(\theta, \phi) = \int_0^{\phi} \int_0^{\theta} F(1 \cdot m, \theta, \phi) d\theta d\phi$$

Final power when integrated from $\theta = 0$ to $\pi/2$ and $\phi = 0$ to 2π is $P = 306$ Watts.

LIST OF REFERENCES

- [1] L. O. R. Storey, *An Investigation of Whistling Atmospherics*, Philosophical Transactions of the Royal Society of London, v. 246, pp. 113-114, 1953.
- [2] R. A. Helliwell, *Whistlers and Related Phenomena*, Stanford University Press, 1965.
- [3] U. S. Inan, *Ionospheric Modification and its Potential to Enhance or Degrade the Performance of Military Systems*, Advisory Group for Aerospace Research & Development, Conference Proceedings No. 485, 1991.
- [4] N. Friedman, *The Naval Institute Guide to World Naval Weapons Systems*, Naval Institute Press, Annapolis, Maryland, 1989.
- [5] L. Boithas, *Radio Wave Propagation*, McGraw-Hill Book Company, 1987.
- [6] W. L. Poulsen, "Modeling of Very Low Frequency Wave Propagation and Scattering within the Earth-Ionosphere Waveguide in the Presence of Lower Ionospheric Disturbances," Ph. D. Dissertation, Stanford University, November 1991.
- [7] J. M. J. Madey, *J. Appl. Phys.* **42**, 1906 (1971); J. M. J. Madey, "Stimulated Emission of Radiation in Periodically Deflected Electron Beam," US Patent 3,822,410, 1974.
- [8] R. W. (Dodge) Warren, and others, "Recent Results from the Los Alamos Free Electron Laser," *Nuclear Instruments and Methods in Physics Research*, **A259**, North-Holland, Amsterdam, 1987.
- [9] J. A. Ratcliffe, *An Introduction to the Ionosphere & Magnetosphere*, Cambridge University Press, 1972.
- [10] D. L. Carpenter and R. L. Smith, "Whistler Measurement of Electron Density in the Magnetosphere," *Reviews of Geophysics*, v. 2, 3, August, 1964.
- [11] U. S. Inan, "Non-Linear Gyro-resonant Interactions of Energetic Particles and Coherent VLF Waves in the Magnetosphere," Ph. D. Dissertation, Stanford University, August, 1977.
- [12] C. R. Carlson, "Siple 21- and 42-kilometer Antennas: Measurement and Performance," *Antarctic Journal*, pp. 270-272, 1983.
- [13] R. A. Helliwell and J. P. Katsufakis, "VLF Wave Injection Into the Magnetosphere from Siple Station, Antarctica, *Journal of Geophysical Research*, **79**, 2511, 1974.

- [14] D. L. Carpenter and A. T. Bao, "Occurrence Properties of Ducted Whistler-Mode Signals from the New VLF Transmitter at Siple, Antarctica, *Journal of Geophysical Research*, 88, 7051, 1983.
- [15] C. A. Balanis, *Antenna Theory: Analysis and Design*, John Wiley & Sons, Inc., 1982.
- [16] John R. Taylor, *An Introduction to Error Analysis: The Study of Uncertainties in Physical Measurements*, University Science Books, 1982.
- [17] J. J. Angerami, "Whistler Duct Properties Deduced from VLF Observations Made with the OGO-3 Satellite near the Geomagnetic Equator," *Journal of Geophysical Research*, 75, 6115, 1970.
- [18] C. R. Carlson and others, "Space-Time Evolution of Whistler-Mode Wave Growth in the Magnetosphere," *Journal of Geophysical Research*, v. 95, A9, 1990.
- [19] F. F. Chen, *Introduction to Plasma Physics and Controlled Fusion*, Volume 1, Plenum Press, New York, 1984.
- [20] U. S. Inan and R. A. Helliwell, "Terrestrial versus Jovian VLF Chorus; A Comparative Study," *Journal of Geophysical Research*, v. 88, A8, 1983.
- [21] R. A. Helliwell and T. L. Crystal, "A Feedback Model of Cyclotron Interaction between Whistler-Mode Waves and Energetic Electrons in the Magnetosphere, " *Journal of Geophysical Research*, v. 78, 31, 1973.
- [22] J. D. Jackson, *Classical Electrodynamics*, 2nd edition, John Wiley and Sons, Inc., 1975.
- [23] W. B. Colson, "Classical Free Electron Laser Theory," Chapter 5 in *Free Electron Laser Handbook*, W. B. Colson, C. Pellegrini, and A. Renieri (eds.), North-Holland Physics, Elsevier Science Publishing Co. Inc., The Netherlands, 1990.
- [24] D. Nunn, "A Self-Consistent Theory of Triggered VLF Emissions, " *Planetary Space Science*, v. 22, pp. 349-378, 1974.
- [25] W. B. Colson and others, "Analogies Between the Free Electron Laser and Whistler Mode Amplification in the Magnetosphere," presented at the 14th Annual Free Electron Laser Conference, Kobe, Japan, 1992.
- [26] W. B. Colson, "Free Electron Laser Theory," Ph. D. Dissertation, Stanford University, 1977.

- [27] W. B. Colson and S. K. Ride, "The Free Electron Laser: Maxwell's Equations Driven by Single-Particle Currents, *Physics of Quantum Electrons*, v. 7, Addison-Wesley Publishing Co., 1980.
- [28] Continuous Electron Beam Accelerator Facility, "High Power UV and IR Free Electron Lasers Using the CEBAF Superconducting Accelerator," Proposal and Technical Description, v. 1, October, 1991.
- [29] G. A. Cord and W. B. Colson, "Comparing Simulations and Experimental Observations of the Trapped-Particle Instability in the Stanford FEL," *Nuclear Instruments and Methods in Physics Research*, North-Holland, A304, 1991.
- [30] D. A. Jaroszynski, R. J. Bakker, A. F. G. van der Meer, D. Oepts, and P. W. van Amersfoort, via private communication, 1992.
- [31] M. A. Shield and L. A. Frank, "Electron Observations Between the Inner Edge of the Plasma Sheet and the Plasmasphere," *Journal of Geophysical Research*, v. 75, 28, October, 1970.
- [32] K. Molvig and others, "Self-Consistent Theory of Triggered Whistler Emissions," *Journal of Geophysical Research*, v. 93, A6, June, 1988.
- [33] L. A. D. Sa, "A Wave-Particle Interaction Mechanism as a Cause of VLF Triggered Emissions," *Journal of Geophysical Research*, v. 95, A8, August, 1990.
- [34] R. A. Helliwell, "A Theory of Discrete VLF Emissions from the Magnetosphere," *Journal of Geophysical Research*, v. 72, 4773, 1967.
- [35] L. R. Lyons and D. J. Williams, *Quantitative Aspects of Magnetospheric Physics*, D. Reidel Publishing Company, Boston, 231, 1984.

INITIAL DISTRIBUTION LIST

- | | |
|--|---|
| 1. Defense Technical Information Center | 2 |
| Cameron Station | |
| Alexandria, Virginia 22304-6145 | |
| 2. Library, Code 52 | 2 |
| Naval Postgraduate School | |
| Monterey, California 93943-5002 | |
| 3. Professor William B. Colson, Code PH/Cw | 7 |
| Department of Physics | |
| Naval Postgraduate School | |
| Monterey, California 93943-5000 | |
| 4. Professor S. Gnanalingam, Code PH/Gn | 1 |
| Department of Physics | |
| Naval Postgraduate School | |
| Monterey, California 93943-5000 | |
| 5. Professor K. E. Woehler, Code PH/Wh | 1 |
| Chairman, Department of Physics | |
| Naval Postgraduate School | |
| Monterey, California 93943-5000 | |
| 6. Professor Vikas S. Sonwalkar | 1 |
| STAR Laboratory, Durand Hall | |
| Department of Electrical Engineering | |
| Stanford University | |
| Stanford, California 94305 | |
| 7. Dr. George Neil | 1 |
| CEBAF | |
| 12000 Jefferson Ave. | |
| Newport News, Virginia 23606 | |

2/6-655

DUDLEY KNOX LIBRARY
NAVAL POSTGRADUATE SCHOOL
MONTEREY CA 93943-5101



GAYLORD S



DUDLEY KNOX LIBRARY



3 2768 00018853 6